# Flow of charged particles in Pb-Pb and pp collisions at the LHC


LUND UNIVERSITY

FACULTY OF SCIENCE

Mohamed Berkat
Supervisor : Peter Christiansen
Division of Particle and Nuclear Physics

Master Thesis

Wednesday 31st January, 2024

# Abstract

In ultra-relativistic heavy-ion collisions, the transition of Quantum Chromodynamic (QCD) matter to a strongly interacting Quark Gluon Plasma (QGP) is a fundamental process where quarks and gluons become deconfined. The expansion of this plasma exhibits characteristics of an ideal relativistic hydrodynamics system, suggesting a behavior similar to that of a perfect fluid. The resulting particles display significant correlations, indicative of collective behavior originating from the QGP phase. One way to investigate the initial conditions and the dynamic evolution of such a collectively expanding medium is by studying the anisotropic flow, quantified by flow coefficients $v_n$.

Previously, small collision system such as pp were used as a benchmark in heavy-ion collisions. However, this perception was questioned due to the observed collective phenomena. Such a behaviour is typically linked to the formation of the QGP in larger systems. The introduction of a novel method to pick up flow in small systems, outlined in this thesis, stems from this open question.

This thesis is dedicated to investigating the elliptic flow harmonic ($v_2$) through the application of various analytical methods, including the Event Plane Method, the Cumulant Method, and a novel approach we sought to introduce. These methodologies are employed in the analysis of collisions at $\sqrt{s_{\mathrm{NN}}} = 2.76$ TeV for Pb-Pb and $\sqrt{s} = 13$ TeV for pp collisions at ALICE experiment at CERN.

The Event Plane Method is utilized to compute the flow coefficients $v_2\{2\}$ for all charged particles, while the Cumulant Method is specifically applied to compute the $v_2\{4\}$. Additionally, we present results for the newly developed method we attempted to implement. This new method allows us to show the presence of flow and anti-flow in *pp* collisions.

# Acknowledgements

I extend my gratitude to Peter, my supervisor, for his patience and engaging discussions on heavy-ion physics. A special thanks goes to Alice for her invaluable assistance in debugging my codes, addressing both straightforward errors and offerings insights into more obscure aspects of ROOT or C++. My appreciation also goes to the PhD students, Joey and Roman, with whom I had the pleasure of sharing an office for a period of time. Their presence contributed to a pleasant working atmosphere. Additionally, I want to express my thanks to all the fellow members of the division and the ALICE group.

# Contents

# 1 Chapter 1

## 1.1 Introduction

The study of high-energy heavy-ion collisions has opened a unique window into the fundamental properties of matter under extreme conditions. These collisions, conducted at relativistic energies, offer a glimpse into a novel phase of matter known as Quark-Gluon Plasma (QGP), a state believed to have existed in the early universe mere microseconds after the Big Bang. Within the QGP, quarks and gluons, the fundamental constituents of matter governed by Quantum Chromodynamics (QCD), are liberated from their hadronic bound states, allowing us to explore their behavior in an entirely new regime.

The primary focus of this thesis revolves around the investigation of specific signals produced by the QGP, specifically the elliptic flow. This phenomenon reveals critical information about the anisotropic expansion of matter. By analyzing the elliptic flow parameter, denoted as $v_2$, for various particle species, including pions, protons, and kaons as a function of transverse momentum ($p_{\mathrm{T}}$), we aim to gain deeper insights into the properties of the created QGP.

The study of the QGP remains an area of ongoing research, and while its existence is well-established, a comprehensive understanding of its properties is still an active pursuit. Various theoretical models, including ideal hydrodynamics and quark recombination, have been proposed to explain the evolution of the QGP system and its imprint on identified particle species. In this thesis, we delve into the analysis of elliptic flow ($v_2$) as a function of transverse momentum and investigate the properties of identified particles.

This chapter serves as an introduction, covering the basics and summarizing key results in heavy ion physics. We then delve into the study of flow-like phenomena in Pb-Pb and p-p collisions. Chapter 3 provides an overview of the LHC, the ALICE experiment, and the relevant detectors used in our analysis. In Chapter 4, we present our results, and Chapter 5 is dedicated to the detailed discussion of these findings. Finally, we wrap up with a summary and a look ahead in the last chapter.

## 1.2 Quantum Chromodynamics (QCD)

Quarks, governed by the Pauli exclusion principle as fermions, exhibit an intriguing characteristic when considered within baryons like $\Omega^-$ ($sss$), possessing a spin of ($J = 3/2$). In this configuration, three valence quarks with identical spins coexist, initially appearing to defy the Pauli exclusion principle. However, this apparent contradiction is resolved through the consideration of the color charge carried by quarks,

introducing an additional degree of freedom within the framework of Quantum Chromodynamics (QCD). Quarks come in three colour states: red, green, and blue, along with their corresponding anticolours for antiquarks. The mediators of the strong force are gluons, which exchange colour charge when interacting with quarks. Gluons, carrying colour, can also interact with other gluons. In total they can have eight colour states. The colour charge of gluons gives birth to a phenomenon known as asymptotic freedom [[7]-[20]]. Similar to the screening effect witnessed in the electromagnetic field, gluons exhibit the capability to fluctuate into a virtual quark-antiquark pair, leading to the induction of a screening effect. This effect shields the original colour charge, resulting in a weakened interaction. However, the self-coupling capability of gluons introduces the possibility of a gluon fluctuating into a virtual gluon-gluon pair. The resultant effect of this, known as antiscreening, surpasses the screening effect. Consequently, quarks exhibit characteristics of free particles at short distances but resist separation. The strength of the strong interaction intensifies as the distance between two quarks approaches the nucleon radius $r \sim 10^{-15}$ m. This phenomenon, known as colour confinement, leads to the confinement of quarks within hadrons under normal conditions. As a consequence, all observed hadrons are colour singlet, or colour neutral. Under normal conditions, these hadrons only exist in bound states, *i.e.* either baryons that consist of three quarks/antiquarks or mesons that consist of a quark-antiquark pair.

## 1.3 Quark-Gluon Plasma (QGP)

Under normal conditions, quarks and gluons are constrained within hadrons. However, under extreme circumstances, such as in the dense core of neutron stars where the density surpasses that of nucleons, a different state of QCD matter emerges. Initially proposed in [8], this scenario posits the creation of a quark soup, wherein quarks and gluons experience deconfinement. A related theory, presented in [9], introduces a critical temperature beyond which conventional hadronic matter cannot exist. The term *quark-gluon plasma* (QGP), coined in [23], now characterizes this highly hot and dense state in which quarks and gluons exists without confinement.

The experimental verification of QGP creation initially occured in the heavy-ion program at the Super Proton Synchrotron at CERN [18], a discovery subsequently confirmed by four experiments at the Relativistic Heavy Ion Collider (RHIC) at BNL [[10]-[5]]. This section will delve into the experimental investigations of QGP through ultra-relativistic collisions of heavy-ions and outlines their evolution.

The QCD phase diagram in Figure 1.1 shows the transition between the hadron gas and the QGP as a function of temperature $T$ and baryon chemical potential $\mu_B$. The domain characterized by low $\mu_B$ and extremely high $T$ is thought to have existed in the very early Universe, immediately following the Big Bang. To explore this epoch, lattice QCD calculations at $\mu_B = 0$ are employed, complemented by experimental findings from ultra-relativistic heavy-ion collisions at the highest energies possible. A key objective of contemporary experiments is to establish constraints on the location of the critical point. The significance of this point lies in its role in the transition between confined and deconfined matter, a transition that varies for regions on either

side of this critical point.

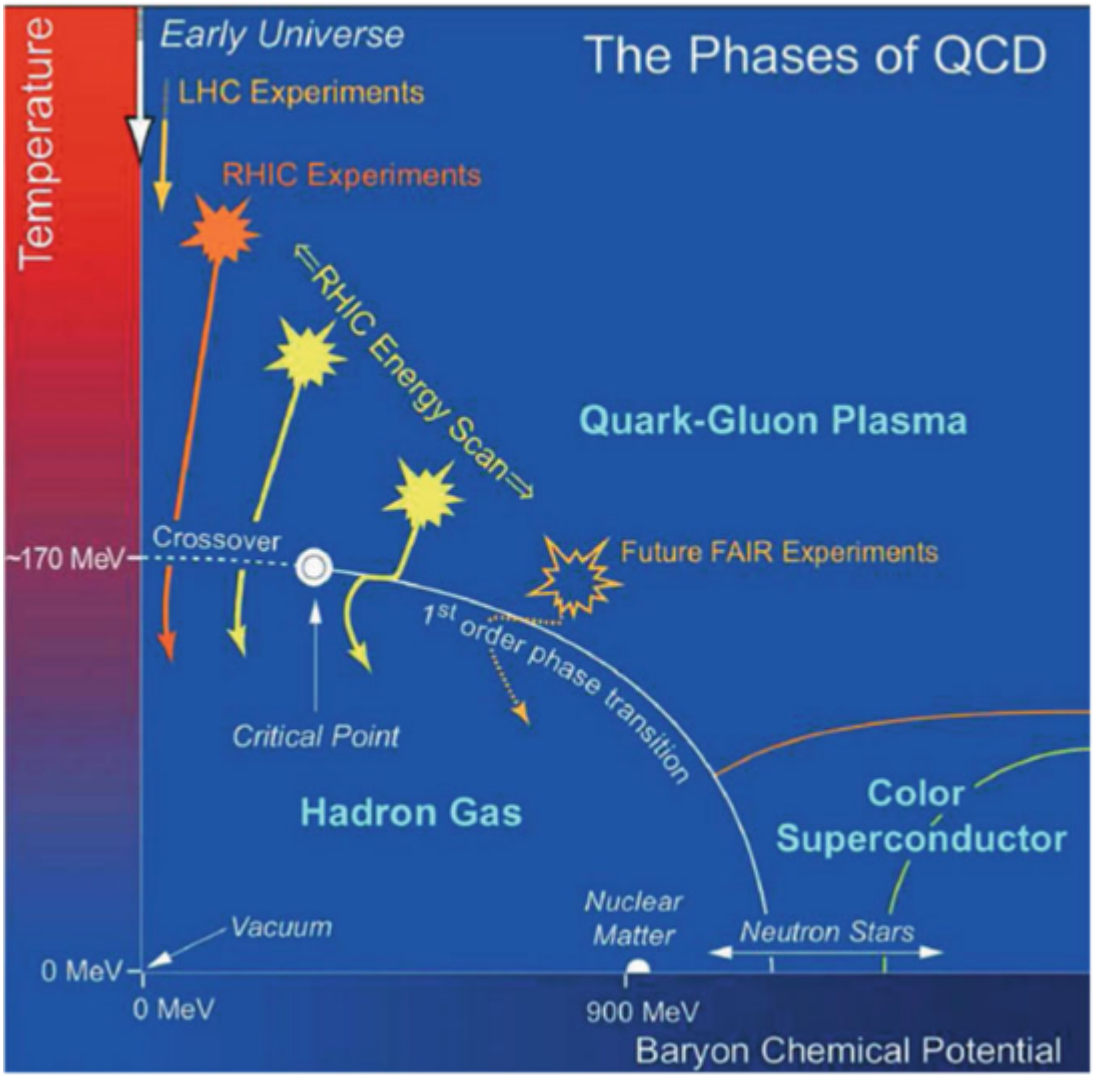


**Figure 1.1:** Scheme of the QCD phase diagram. Taken from [6].

## 1.4 Evolution of a heavy-ion collision

When accelerated to ultra-relativistic energies, heavy nuclei undergo Lorentz contraction, as depicted in the first panel of 1.2. The impact parameter $b$, representing the distance between the centres of the colliding nuclei, characterizes the collision geometry. A small $b$ corresponds to central collisions, whereas larger $b$ denotes peripheral collisions. In these collisions, only participant nucleons actively engage, while spectators persist in their original direction along the beam axis. The determination of the number of participants and spectators is crucial, as it is closely linked to $b$, a parameter that proves to be challenging to experimentally ascertain.

In addition to the impact parameter $b$, the arrangement of nucleons within the colliding nuclei significantly influences the initial collision geometry. This distribution

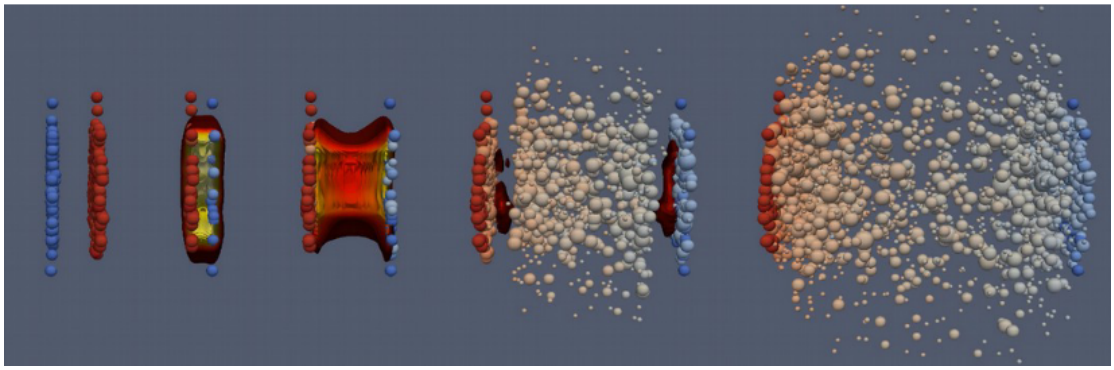

**Figure 1.2:** Different stages of the space-time evolution of a heavy-ion collision. (H. Petersen 2022)

is aptly described by the Woods-Saxon nuclear density potential [17]. This distribution varies event-by-event. The collision geometry, determined by e.g. the nucleons arrangement at the moment of collision and the impact parameter, influences the intial state of the collisions.

Immediately following the collision, the phase of pre-equilibrium dynamics unfolds, at $\tau \lesssim 1$ fm/$c$ [19]. During the initial interactions at $\tau \sim 0$, hard scattering processes occur, generating partons characterized by large transverse moment $p_T$ or large masses. Jets stemming from high $p_T$ partons are denoted as hard probes. These hard probes play a pivotal role in QGP studies since they form before the QGP itself.

Following the pre-equilibrium phase, a state of local equilibrium is established through thermalization within the deconfined QCD matter, giving rise to the formation of the QGP. Once the equilibrated QGP has been formed, the precise evolution of the QGP can be accurately described through relativistic hydrodynamics. One of the main experimental results from RHIC and the LHC is that the QGP exhibits characteristics akin to those of a nearly ideal fluid.

While the QGP undergoes rapid expansion and cooling, a hadronization process occurs when the local temperature becomes of the order of the critical temperature, $T \sim T_c$, transforming all quarks and gluons into hadrons. These newly formed hadrons retain the ability to interact both elastically and inelastically for a brief period. Following further expansion, the system attains a local chemical equilibrium and no further inelastic scattering takes place; stabilizing the yields of all the hadrons.

Ultimately, the kinetic freeze-out happens when all hadronic scatterings conclude, and the momentum of the particles stabilizes. Beyond this point, particles persist on their trajectory towards the detector, where heavier particles decays, transitioning into longer lived particles. Subsequently, these particles have the potential to interact with the detector enabling their detection.

## 1.5 Studying the QGP: Collective flow

A heavy-ion collision is not a mere superposition of numerous nucleon collisions. The resulting strongly interacting QCD matter, the QGP, manifests nearly ideal fluid-like behavior, and evolves hydrodynamically as a bulk. The coordinated motion of particles within this medium is named *collective flow*.

Radial flow serves as a key indicator of the transverse expansion within the QGP. In more central collisions, the generated QGP fireball undergoes isotropic and longer expansion compared to peripheral collisions, resulting in heightened radial flow [22]. Additionally, the influence of radial flow is more pronounced on heavier particles [6].

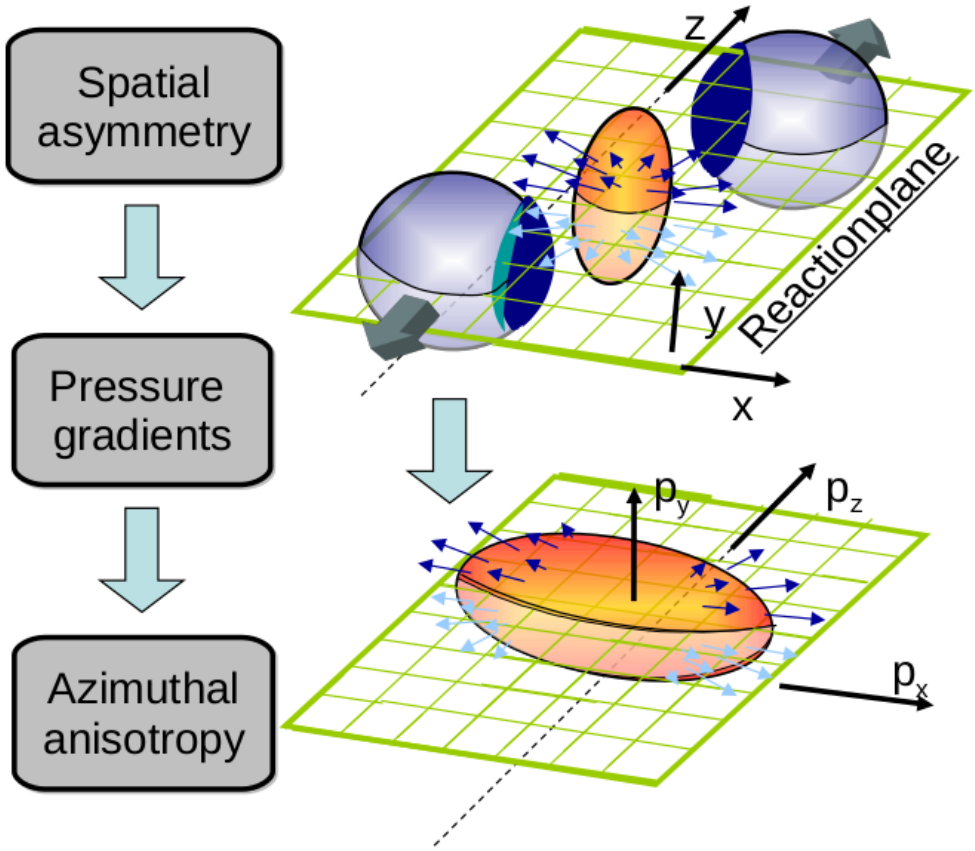


**Figure 1.3:** illustration of non-central heavy-ion collision and the subsequent expansion of the created medium. Taken from [6]

Beyond radial flow, prevalent in central collisions, another noteworthy phenomenon in heavy-ion collisions is anisotropic flow, as illustrated in Figure 1.3. The initial geometry, characterized by the overlap between colliding heavy nuclei, often assumes an ellipsoidal shape, quantifiable by its eccentricity :

$$\epsilon = \frac{\langle y^2 + x^2 \rangle}{\langle y^2 - x^2 \rangle} \tag{1.1}$$

This initial azimuthal anisotropy induces disparate pressure gradients within the expanding medium. Consequently, a collective motion of all produced partons is enhanced preferentially along the horizontal axis, leading to observable momentum anisotropy in the final state. Due to its origin in the ellipsoid shape, it is referred to as elliptic flow.

In general, anisotropic flow can be characterized using various harmonics $n$ of flow coefficients $v_n$; with the first three harmonics termed directed, elliptic and triangular flow, respectively. Furthermore, the collective behaviour can be investigated through two-dimensional di-hadron correlations. The correlation function $C(\Delta\eta, \Delta\phi)$ can serve as a tool to extract flow coefficients, and an illustrative example of $C(\Delta\eta, \Delta\phi)$ in Pb-Pb collsions is presented in Figure 1.4. The configuration of $C(\Delta\eta, \Delta\phi)$ is dependent on centrality. This correlation function can be divided into two regions - near-side at $|\Delta\phi| < \pi/2$, and away-side at $\pi/2 < \Delta\phi < 3\pi/2$. Notably, around $(\Delta\eta, \Delta\phi) \approxeq (0, 0)$, a peak of near-side jet that originates from correlations of particles in the same jet is more visible towards the peripheral collisions. In contrast, only a subtle indication of this peak is observed in central collisions. The away-side peak, arising from correlations among particles from opposite jets, is discernible accross all centralities.

The aforementioned near-side ridge in heavy-ion collisions is connected with the collective expansion and hydrodynamic evolution of the produced QCD medium. The measurement shown in [2] provided the first hint of collective behaviour in small collision systems with a visible ridge. This prompts an inquiry into the potential formaiton of q QGP in these systems. Similar to large collision systems, where measurements of anisotropic flow played a crucial role in uncovering the existence of QGP, this obersable - expressed through flow coefficients- is chosen to investigate anisotropic collectivity in smaller systems.

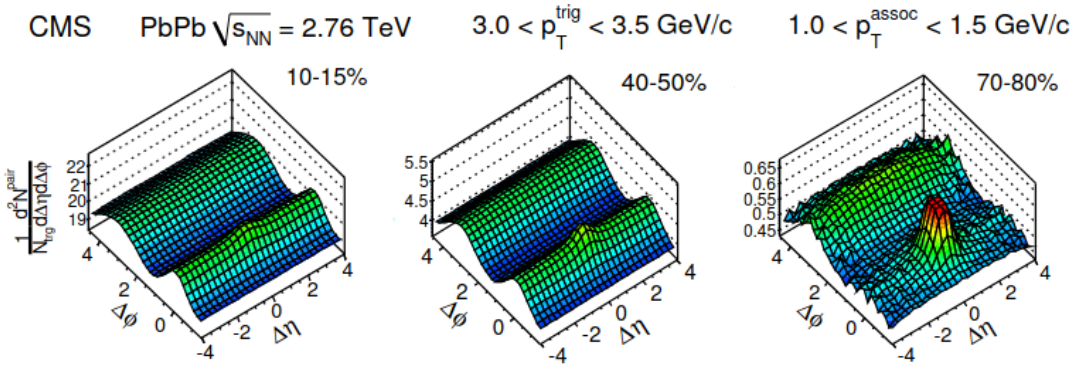


**Figure 1.4:** Correlation function $C(\Delta\eta, \Delta\phi)$ in Pb-Pb collisions at $\sqrt{s_{\mathrm{NN}}} = 2.76\,\mathrm{TeV}$ taken from [1].

# 2 Experimental Setup

Established in 1954, the Conseil Européen pour la Recherche Nucléaire (CERN), a research institution located in Switzerland, marked a historic milestone as Europe's pioneering collaborative effort in the realm of scientific research. Currently, CERN boasts a consortium of 20 member states united by a common commitment to advancing the frontiers of fundamental particle physics [14]. The cornerstone of CERN's mission is the exploration of particle physics, exemplified by its hosting of the world's largest particle accelerator, the Large Hadron Collider (LHC), introduced below.

## 2.1 The Large Hadron Collider

Serving as the beating heart of particle physics, the Large Hadron Collider (LHC) resides within the expansive 27-kilometer circular tunnel once utilized by the Large Electron–Positron Collider (LEP) accelerator. The orchestration of the LHC's particle acceleration process necessitates the involvement of a series of pre-accelerators. Initially, protons and lead (Pb) ions embark on their journey through a linear accelerator, followed by a series of three successive synchrotron accelerators. Once these accelerated particles are ushered into the final LHC ring, they are strategically divided into two separate beams, with one traversing the tunnel in a clockwise direction while its counterpart journeys in a counterclockwise path. These two beams collide at four distinct junctures, each serving as the exclusive domain for one of the LHC's four flagship experiments: A Toroidal LHC Apparatus (ATLAS), the Large Ion Collider Experiment (ALICE), the Compact Muon Solenoid (CMS), and the Large Hadron Collider beauty (LHCb). Each of these experiments maintains a unique scientific focus and operates in close collaboration with dedicated research teams around the world. This chapter centers on the ALICE detector, and consequently, a more comprehensive description of this specific detector will follow.

## 2.2 ALICE

ALICE stands as the exclusive heavy-ion research endeavor at the LHC, an international collaboration comprising 170 research institutes spanning 40 countries. Its central mission revolves around probing the properties of strongly-interacting matter under extraordinary conditions characterized by elevated temperature and energy density. The ALICE detector boasts dimensions of $26m \times 16m \times 16m$ and a considerable weight of 10,000-tonne. This detector includes a central barrel, meticulously engineered for the measurement of hadrons, electrons, and photons, alongside a forward muon spectrometer, and a suite of specialized detectors.

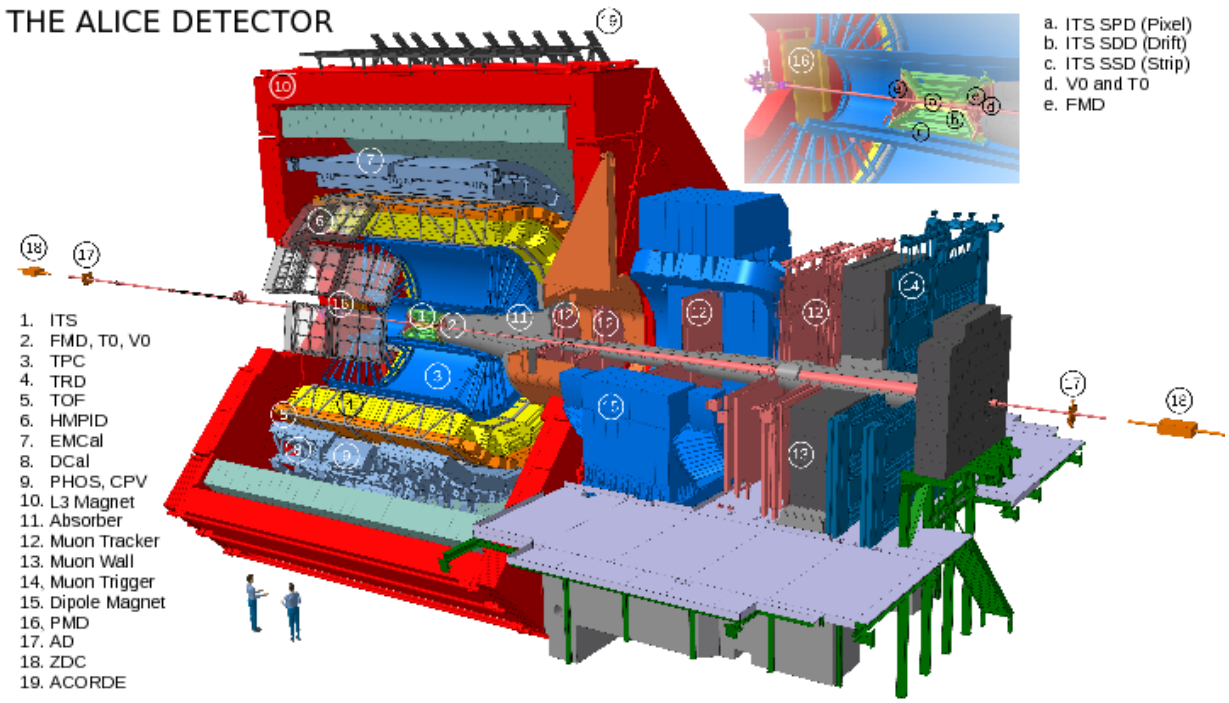


**Figure 2.1:** Scheme of ALICE experiment for LHC Run 2.

Nestled beneath the surface, the heart of the ALICE experiment operates at a depth of 44 meters. From its inception, ALICE was designed with Particle Identification (PID) as a primary objective. Moreover, it was crafted in anticipation of the substantial particle multiplicities expected from prior heavy-ion experiments, thus optimizing its capabilities for measuring precisely individual tracks even for large charged particle multiplicity densities.

In addition to measuring particles' momenta (p) across a wide spectrum, ranging from several tens of MeV/c to over 50 GeV/c, the detector also records specific ionization energy loss (dE/dx), time-of-flight (TOF) information, transition radiation, and Cherenkov radiation. ALICE is further equipped with electromagnetic calorimetry, muon filters, and topological decay reconstruction, encompassing most of established Particle Identification (PID) techniques.

Beginning from the innermost layer and progressing outward, the heart of the ALICE detector encompasses a series of key components, with our primary focus for this thesis analysis honing in on two pivotal elements: the Inner Tracking System (ITS) and the cylindrical Time-Projection Chamber (TPC).

The primary functions of the Inner Tracking System (ITS) involve the reconstruction of both primary and secondary vertices, as well as the tracking and identification of charged particles with a low transverse momentum ($p_{\mathrm{T}}$) cutoff. Additionally, the system aims to enhance momentum resolution at high $p_{\mathrm{T}}$.

The ITS1, used in this thesis, is a composite structure comprising three distinct detector systems, arranged in order of increasing distance from the beam pipe. These are the Silicon Pixel Detectors (SPD), the Silicon Drift Detectors (SDD), and the Silicon micro-Strip Detectors (SSD). Spanning a pseudo-rapidity range of $|\eta| < 1.98$, the ITS

plays a crucial role in the accurate analysis of particle behavior. Following the second Long Shutdown of the LHC (2019-2021), a state-of-the-art ultra-light, high-resolution ITS -the ITS2- has been implemented. This upgraded system has significantly enhanced tracking precision and efficiency at low-transverse momenta. Notably, the readout pixel pitch has been reduced to approximately $30 \times 30\mu m^2$, resulting in a total of about 12.5 Giga pixels covering an active surface area of approximately $10m^2$.

The ALICE Time Projection Chamber (TPC) serves as the primary instrument for tracking charged particles and conducting particle identification within the central barrel of the ALICE detector. Specifically designed to handle the highest achievable multiplicities of charged particles resulting from central Pb-Pb collisions, the TPC has an azimuthal angle acceptance of $2\pi$ and spans a pseudo-rapidity range of $|\eta| < 0.9$. This gas-filled cylindrical chamber features a central hole to accommodate the silicon tracker and beam pipe, with ionizing radiation-induced charges projected onto detectors positioned in the two endplates. These detectors employ Multiwire Proportional Chamber (MWPCs), for signal amplification.

As charged particles traverse the TPC volume, they ionize the gas, releasing electrons that drift towards the cylinder's endplates. The Gas Electron Multipliers, configured in an optimized multilayer setup, provide the necessary signal amplification. Stringent requirements to control ion-induced space-charge distortions set a 2% upper limit for fractional ion backflow at the operational gas gain of 2000 in a Ne-$CO_2$-$N_2$ (90-10-5) gas mixture. Simultaneously, the readout system delivers a local energy resolution better than 14% at the $^{55}$Fe-peak, meeting the required dE/dx resolution of the TPC. The TPC significantly contributes to the PID process, which is done via the knowledge of the total energy loss per unit path length of a specific particle species. It is described by the Bethe-Bloch formula:

$$\left\langle \frac{dE}{dx} \right\rangle \propto -\frac{1}{\beta^2} ln\left(\beta^2\gamma^2 - \beta^2\right) \tag{2.1}$$

where the $\beta$ is the particle velocity and $\gamma$ is the relativistic Lorentz factor [16].

The active gas volume holds an aluminized Mylar foil at its center, perpendicular to the beam axis. To maintain a constant voltage gradient of $400V/cm$ towards the detector ends, a high voltage of $100kV$ is applied to the central foil. Precise timing measurements, combined with knowledge of the constant drift velocity, enable the three-dimensional trajectory reconstruction of all charged particles traversing the TPC.

V0 is made of two arrays of scintillator counters set on both sides of the ALICE interaction point, and called V0-A and V0-C. The V0-C counter is located upstream of the dimuon arm absorber and covers the spectrometer acceptance while the V0-A counter is located at around 3.4 m away from the collision vertex, on the other side. The V0-A covers a pseudo-rapidity range of $2.8 < \eta < 5.1$, while the V0-C covers the interval $-3.7 < \eta < -1.7$ [15]. It is used to estimate the centrality of the collision by summing up the energy deposited in the two disks. This observable scales directly with the number of primary particles generated in the collision and therefore to the centrality. V0 can also measure the luminosity in $pp$ collision and help eliminate background events.

## 2.3 Offline software framework

The ALICE offline software framework has been developed in order to reconstruct and analyse the data coming both from simulated and real collisions. This framework is dubbed AliROOT, and has been built on top of ROOT. The ROOT system is an object-oriented framework written in C++ developed at CERN since the 90's, [21] and used by various collaborations worldwide as a starting framework on top of which the specific framework needed for particular collaboration is being built. It provides a full set of features needed for event generation, detector simulation, event reconstruction, data acquisition and data analysis. A vast majority of ROOT classes inherit from the common base called TObject, which provides default behaviour and protocol (error handling, sorting, inspecting, drawing, etc.).

# 3 Analysis Method

The primary objective of this thesis is to investigate the elliptic flow of identified hadrons in Pb-Pb and p-p collisions across various centralities. This exploration is conducted through established techniques such as the Event-Plane Method and 2-particle correlations. Notably, a novel method, rooted in the correlations observed within the jet cone, takes center stage as a focus for our later study. There are several ways to measure the elliptic flow. In the first method, one attempts to realign each event to the reaction plane, while in the second method, one studies 2-particles correlations. We will use the word *event* to denote a single heavy-ion collision, *track* and *particles* interchangeably, to indicate the particles measured in each event.

## 3.1 The Event-Plane Method

The reaction plane will vary event-by-event and will take on any angle with equal probability. The essence of the Event-Plane (EP) Method lies in the estimation of the reaction plane for each event and subsequently examining the distribution of azimuthal angles for the tracks relative to this plane. When the reaction plane can be accurately determined for an event, the relative angles between particles become independent of the actual orientation of the reaction plane. Consequently, this permits the aggregation of results across numerous events, ensuring precise measurements of the distribution.

Quantitatively, anisotropic flow is characterized by coefficients in the Fourier expansion of the azimuthal dependence of the invariant yield of particles relative to the reaction plane:

$$E\frac{d^3N}{d^3p} = \frac{1}{2\pi}\frac{d^2N}{p_t dp_t dy}\left(1 + \sum_{n=1}^{\infty} 2v_n \cos(n(\phi_n - \Psi_R))\right) \tag{3.1}$$

Where $E$ is the energy of the particle, $p_{\mathrm{T}}$ is the transverse momentum, $\phi$ is the azimuthal track angle, $y$ is the rapidity and $\Psi_R$[1] the reaction plane angle. The coefficient $v_2$ is called *elliptic flow*.

The $2^{nd}$ symmetry plane constructed by the reaction plane $\Psi_2$ can be estimated by the azimuthal distribution of particles. It serves as a proxy of the reaction plane. This reaction plane is not measurable in practice. In order to solve this, one can reconstruct $\phi - \Psi_2$ (See Appendix A). From equation 3.1, $\Psi_2$ can be estimated as:

$$\Psi_2 = \frac{1}{2}\arctan\left(\frac{<\sin(2\phi)>}{<\cos(2\phi)>}\right) \tag{3.2}$$

[1]The expression in equation 3.1 is dated, but it remains useful in the scope of this thesis.

Here, $\langle X \rangle$ denotes the average of $X$ over all tracks in a single event. Following measurement across multiple events, the final histogram of all azimuthal angles relative to this plane can be fitted using 3.3:

$$\frac{dN}{d(\phi - \Psi_2)} = C(1 + 2v_2 \cos[2(\phi - \Psi_2)]) \tag{3.3}$$

In this equation, $C$ represents the normalization constant, which corresponds to the total number of tracks divided by the number of bins in the histogram. The term $v_2\{EP\}$ is then used to denote the elliptic flow measured through this approach.

## 3.2 2-particles correlations method

The Event-Plane Method faces criticism due to the necessity of initially determining the event plane before measuring $v_2$. The statistical precision in determining the event plane on an event-by-event basis can impact the final result. An alternative approach to circumvent this issue involves the study of 2-particle correlations.

However, delving into multi-particle correlations introduces a challenge in terms of computational requirements, especially when considering all possible particle multiplets. This limitation practically hinders the calculation of correlations beyond order $k = 3$. To address this computational challenge, a solution proposed in [11] involves expressing cumulants in terms of moments of the magnitude of the corresponding flow vector $Q_n$, defined as in equation 3.4.

$$Q_n \equiv \sum_{i=1}^{M} e^{in\phi_i} = \left( \sum_{i=1}^{M} \cos(n\phi_i) \right) + i \left( \sum_{i=1}^{M} \sin(n\phi_i) \right) = Q_x + iQ_y, \tag{3.4}$$

Where $M$ is the number of particles.

This method provides a more computationally feasible way for studying correlations in high-order particle multiplets.

In this section of the thesis, our focus will primarily be on 2-particle azimuthal correlations. However, the extension to azimuthal correlations involving more particles is straightforward. To derive these correlations, the process involves averaging over all particles within a given event and subsequently averaging over all events. The latter averaging may incorporate weights based on event multiplicity.

The definition of *single-event* average 2-particle azimuthal correlations follows the approach outlined in [12]:

$$\langle 2 \rangle \equiv \left\langle e^{in(\phi_1 - \phi_2)} \right\rangle \equiv \frac{1}{P_{M,2}} \sum_{i=1}^{M} \sum_{j=1, j \neq i}^{M} e^{2i(\phi_i - \phi_j)}, \tag{3.5}$$

where $P_{n,m} = n!/(n-m)!$.

The 2-particle azimuthal correlation can then be calculated in two steps:

$$\langle 2 \rangle = \frac{|Q_2|^2 - M}{M(M-1)}, \tag{3.6}$$

Then the second step involves averaging over all events:

$$\langle\langle 2 \rangle\rangle = \left\langle \left\langle e^{in(\phi_1 - \phi_2)} \right\rangle \right\rangle = \frac{\sum_{events} \left(W_{\langle 2 \rangle}\right)_i \langle 2 \rangle_i}{\sum_{events} \left(W_{\langle 2 \rangle}\right)_i} \tag{3.7}$$

Where by double brackets we denote an average, first over all particles and then over all events. $\left(W_{\langle 2 \rangle}\right)_i$ are the event weights used to minimize the effect of multiplicity variations in the event sample on the estimates of 2-particles correlations. In this part of the thesis, we suppose that $v_n$ is independent of multiplicity, we use: $W_{\langle 2 \rangle} \equiv M(M-1)$. Using the formalism of cumulants introduced by Ollitrault *et al* in [13], the $2^{nd}$ order cumulant, $c_n\{2\}$ is simply an average of 2-particles correlation:

$$c_2\{2\} = \langle\langle 2 \rangle\rangle \tag{3.8}$$

The elliptic flow obtained from 2-particles correlations can then be derived as:

$$v_2\{2\} = \sqrt{c_2\{2\}} \tag{3.9}$$

### 3.2.1 Extension to 4-particles

The starting point is to define 4-particles azimuthal correlation:

$$\langle 4 \rangle \equiv \left\langle e^{in(\phi_1 + \phi_2 - \phi_3 - \phi_4)} \right\rangle \equiv \frac{1}{P_{M,4}} \sum_{i,j,k,l}{}' e^{in(\phi_i + \phi_j - \phi_k - \phi_l)}, \tag{3.10}$$

Where the prime in the sum $\sum'_{i,j,k,l}$ means that all indices in the sum must be taken different.

To obtain the $4^{th}$ order cumulant we start with the decomposition of $|Q_n|^4$:

$$|Q_n|^4 = Q_n Q_n Q_n^* Q_n^* = \sum_{i,j,k,l}^{M} e^{in(\phi_i + \phi_j - \phi_k - \phi_l)} \tag{3.11}$$

There exist four distinct cases for $i, j, k, l$:

- They are all different $\Rightarrow$ 4-particles correlations,
- Three are different $\Rightarrow$ mixed harmonics 3-particles correlations,
- Two are different,
- They are all the same.

Hence, the analytic result for the single-event average 4-particles correlation is:

$$\langle 4\rangle = \frac{|Q_n|^4 + |Q_{2n}|^2 - 2\cdot\Re[Q_{2n}Q_n^*Q_n^*]}{M(M-1)(M-2)(M-3)} - 2\frac{2(M-2)\cdot|Q_n|^2 - M(M-3)}{M(M-1)(M-2)(M-3)} \tag{3.12}$$

Averaging over $N$ events yields:

$$\langle\langle 4\rangle\rangle = \left\langle\left\langle e^{in(\phi_1+\phi_2-\phi_3-\phi_4)}\right\rangle\right\rangle = \frac{\sum_{events}\left(W_{\langle 4\rangle}\right)_i\langle 4\rangle_i}{\sum_{events}\left(W_{\langle 4\rangle}\right)_i} \tag{3.13}$$

We use: $W_{\langle 4\rangle} \equiv M(M-1)(M-2)(M-3)$

As was pointed out above, the 4-particles correlation, (i.e. 4-particle cumulant), is then given by:

$$c_2\{4\} = \langle\langle 4\rangle\rangle - 2\langle\langle 2\rangle\rangle^2 \tag{3.14}$$

And finally the elliptic flow obtained from 4-particles correlations can be derived as:

$$v_2\{4\} = \sqrt[4]{-c_2\{4\}} \tag{3.15}$$

## 3.3 Differential flow

Once the reference flow has been estimated with the help of the formalism from the previous section, we proceed to the calculation of the differential flow. For that, all particles selected for flow analysis are labeled as *Reference Flow Particles*, RFP, and/or *Particle Of Interests*, POI. In the first step, one estimates the reference flow by using only the RFPs, while in the second step, we estimate the differential flow of POIs with respect to the reference flow of the RFPs obtained in the first step.

### 3.3.1 Reduced multi-particle azimuthal correlations

For reduced single-event average 2- and 4-particle azimuthal correlations, by which we mean to indicate that one particle in the correlator, usually the POIs is restricted to belong only to the narrower phase-space window, e.g. to the narrower transverse momentum range, we use the following definition:

$$\langle 2'\rangle \equiv \left\langle e^{in(\psi_1-\phi_2)}\right\rangle = \frac{1}{m_pM - mq}\sum_{i=1}^{m_p}\sum_{j=1}^{M}{}' e^{in(\psi_i-\phi_j)} \tag{3.16}$$

$$\langle 4'\rangle \equiv \left\langle e^{in(\psi_1+\phi_2-\phi_3-\phi_4)}\right\rangle = \frac{1}{(m_pM-3mq)(M-1)(M-2)}\sum_{i=1}^{m_p}\sum_{j,k,l=1}^{M}{}' e^{in(\psi_i+\phi_j-\phi_k-\phi_l)} \tag{3.17}$$

where $m_p$ is the total number of particles labeled as POI (some of which might have been also labeled additionally as RFP), $m_q$ is the total number of particles labeled *both* as RFP and POI, $M$ is the total number of particles labeled as RFP (some of which might have been also labeled as POI) in the event, $\psi_i$ is the azimuthal angle of the $i$-th particle labeled as POI and taken from the phase window of interest (taken even if it was also additionally labeled as RFP), $\phi_j$ is the azimuthal angle of the $j$-th particle labeled as RFP (taken even if it was also additionally labeled as POI). The second sum is taken with all indices taken different.

Finally, event averaged reduced 2- and 4-particles correlations are given by:

$$\langle\langle 2' \rangle\rangle \equiv \frac{\sum_{events} \left(w_{\langle 2' \rangle}\right)_i \langle 2' \rangle_i}{\sum_{events} \left(w_{\langle 2' \rangle}\right)_i} \tag{3.18}$$

$$\langle\langle 4' \rangle\rangle \equiv \frac{\sum_{events} \left(w_{\langle 4' \rangle}\right)_i \langle 4' \rangle_i}{\sum_{events} \left(w_{\langle 4' \rangle}\right)_i} \tag{3.19}$$

In this thesis we use events weights $w_{\langle 2' \rangle}$ and $w_{\langle 4' \rangle}$ defined by:

$$w_{\langle 2' \rangle} \equiv m_p M - m_q \tag{3.20}$$

$$w_{\langle 4' \rangle} \equiv (m_p M - 3m_q)(M-1)(M-2) \tag{3.21}$$

As in the case of reference flow, this choice for the event weights reflects the number of distrinct combinations of particles one can form when calculating the average reduced 2- and 4-particles correlations.

### 3.3.2 Differential cumulants

We derive equations for the differential cumulants using $p$ and $q$ vectors; the former built out of all POIs ($m_p$ in total), and the second only from POI labeled also as RFP ($m_q$ in total):

$$p_n \equiv \sum_{i=1}^{m_p} e^{in\psi_i} \tag{3.22}$$

$$q_n \equiv \sum_{i=1}^{m_q} e^{in\psi_i} \tag{3.23}$$

The $q$-vector is introduced here in order to subtract effects of autocorrelations. Using those, we obtain the following equations for the average reduced single- and all-event 2-particle correlations:

$$\langle 2' \rangle = \frac{p_n Q_n^* - m_q}{m_p M - m_q}, \tag{3.24}$$

$$\langle\langle 2' \rangle\rangle = \frac{\sum_{events} \left(w_{\langle 2' \rangle}\right)_i \langle 2' \rangle_i}{\sum_{events} \left(w_{\langle 2' \rangle}\right)_i} \tag{3.25}$$

For detectors with uniform azimuthal acceptance the differential $2^{nd}$ order cumulant is given by:

$$d_n\{2\} = \langle\langle 2' \rangle\rangle \,, \tag{3.26}$$

Estimates of differential flow $v'_n$ are denoted as $v'_n\{2\}$ and are given by:

$$v'_n\{2\} = \frac{d_n\{2\}}{\sqrt{c_n\{2\}}} \tag{3.27}$$

In the ideal case scenario when only flow correlations are present, the numerator in equation above gives $v'_n v_n$, while the denominator gives $\sqrt{v_n v_n}$, so that the reference flow harmonic $v_n$ drops out from equation 3.27. The point behind the usage of reference particles is only to make statistically stable both numerator and denominator in equation 3.27, i.e. direct differential flow analysis using only particles of interest would not be feasible in practice due to limited statistics of particles of interests in majority of the case. For this reason, reference particles are always selected to be the most abundant particles in an event, usually all charged particles.

Below we present the corresponding formulae for reduced 4-particles correlations:

$$\begin{aligned} \langle 4' \rangle = & [p_n Q n_n Q_n^* Q_n^* - q_{2n} Q_n^* Q_n^* - p_n Q_n Q_{2n}^* \\ & -2 \cdot M p_n Q_n^* - 2 \cdot |Q_n|^2 + 7 \cdot q_n Q_n^* \\ & -Q_n q_n^* + q_{2n} Q_{2n}^* + 2 \cdot p_n Q_n^* + 2 \cdot m_q M - 6 m_q] \\ & / \left[(m_p M - 3 m_q)(M-1)(M-2)\right] \end{aligned} \tag{3.28}$$

$$\langle\langle 4' \rangle\rangle = \frac{\sum_{events} \left(w_{\langle 4' \rangle}\right)_i \langle 4' \rangle_i}{\sum_{events} \left(w_{\langle 4' \rangle}\right)_i} \tag{3.29}$$

Then the $4^{th}$ order differential cumulant is given by :

$$d_n\{4\} = \langle\langle 4' \rangle\rangle - 2 \cdot \langle\langle 2' \rangle\rangle \langle\langle 2 \rangle\rangle \tag{3.30}$$

With which we can estimate the differential flow:

$$v'_n\{4\} = -\frac{d_n\{4\}}{(-c_n\{4\})^{3/4}} \tag{3.31}$$

This $p_{\mathrm{T}}$-differential flow can be studied for different particle species, as presented in 5.

## 3.4 New approach to pick up flow of underlying events in *pp*

The collective behaviour can be studied using two-dimensional di-hadron correlations. The two-particle correlation observable measured here is the correlation function $C(\Delta\phi, \Delta\eta)$, where the pair angles $\Delta\phi$ and $\Delta\eta$ are measured with respect to the trigger particle. This new method that we aimed to develop in this thesis revolves around the understanding of the ridge observed in [2] in *pp* collisions, which is a phenomenon that is seen as a reflection of collective flow. Our aim was to understand whether it emerges from collective hydrodynamic behaviour or if it is generated by semi-hard processes. If it is the latter, then actively selecting/rejecting events with low $p_{\mathrm{T}}$ jets should enhance/weaken this ridge. In order to achieve that, we need to ensure that the event activity is not biased by the presence of jets to the best of our ability. We identified an optimal range for the $p_{\mathrm{T}}$ of the trigger, aiming for a low value to maximize the statitics. However, it is crucial to maintain a sufficiently high $p_{\mathrm{T}}$ for the trigger to prevent any undesired flow effects.

The idea was to employ a constrained cone shape around a trigger on a high $p_{\mathrm{T}}$ particle with $6 < p_{\mathrm{T}} < 8$ GeV which allows us to capture the signal, primarily associated with the flow of underlying events. We validate that the trigger does not flow by looking at 2-particle correlations with associated particles ($0.5 < {p_{\mathrm{T}}}^{a} < 3$ GeV/c) for large distances in pseudorapidity $\Delta\eta = |\eta^t - \eta^a|$, to avoid contamination from the jet on the near-side peak. Then, we defined a cone around the trigger in $\Delta\eta$ and $\Delta\varphi = \varphi^t - \varphi^a$. The goal is to pick up non-jet particles. Then we calculate the jet $p_{\mathrm{T}}$ as the sum of the $p_{\mathrm{T}}$ in the cone. Now we expect that if we cut on a certain jet $p_{\mathrm{T}}$ we will start to see that for jet $p_{\mathrm{T}}$ above the cut we will see flow, as we pick up flowing particles in the underlying events, and for jet $p_{\mathrm{T}}$ below we see antiflow since the whole jet should not flow. The projection of $C(\Delta\phi, |\Delta\eta| > 0.9)$ into $\Delta\phi$ is studied in section 5.

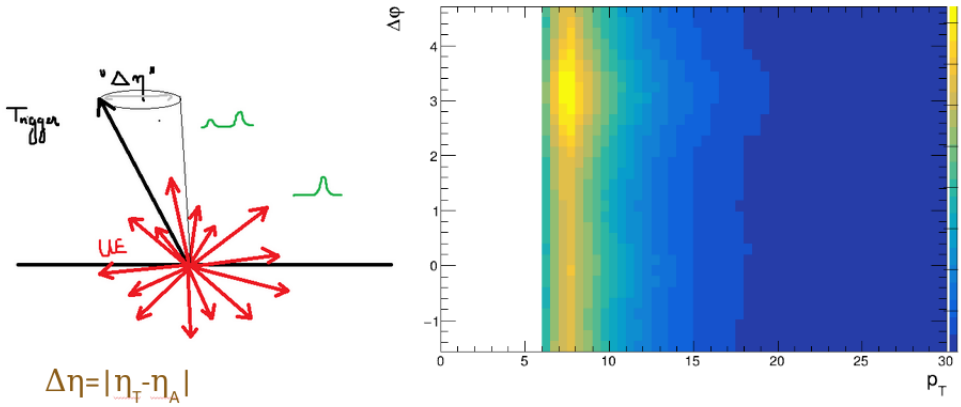


**Figure 3.1:** Representation of the new method to pick up flow of underlying events in *pp*. The idea is to actively go from a two-bumps plots to a one-bump plot, representing the projection of the 2D histogram on the $\Delta\varphi$ axis.

# 4 Analysis procedure

The data used for the Pb-Pb analysis were recorded in November 2010 during the first run with heavy ions at the LHC. For this analysis the ALICE ITS and the TPC were used to reconstruct the charged particle tracks. The V0 counters and the SPD were used for the trigger. The V0 counters are two scintillator arrays providing both amplitude and timing information, convering the pseudorapidity range $2.8 < \eta < 5.1$ (V0A) and $-3.7 < \eta < -1.7$ (V0C). Only events with a vertex found in $|z| < 10$cm were used in this analysis to ensure a uniform acceptance in the central pseudorapidity region $|\eta| < 0.8$. The data are analyzed in different centrality classes determined y cuts on the uncorrected charged particle multiplicity.

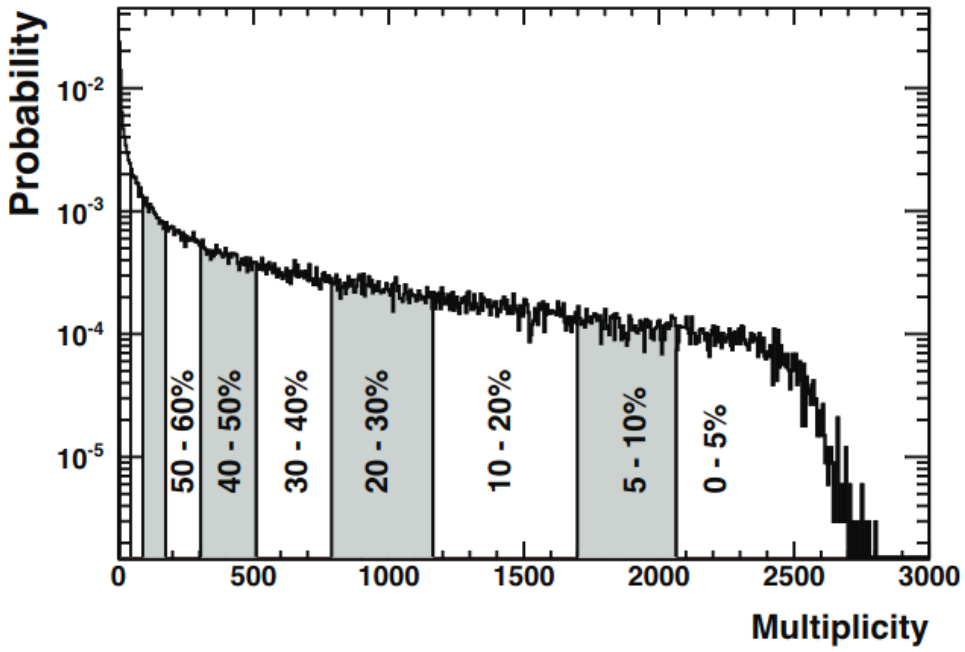


**Figure 4.1:** The uncorrected multiplicity distribution of charged particles in the TPC for $|\eta| < 0.8$. The centrality bins used in the analysis are shown and the cumulative fraction of the total events is indicated in percent except for 60-70% and 70-80%.

The data used for the *pp* analysis were recorded between 2017 and 2018. The V0 counters were used and had the following pseudorapity ranges : $2.8 < \eta < 5.1$ (V0A) and $-3.7 < \eta < -1.7$ (V0C).

# 5 Results and discussion

## 5.1 $v_2$ coefficient through the Event Plane Method

The reconstruction of $\varphi - \Psi_2$ is showcased for different transverse momentum ranges and centrality levels. Figures 5.2, 5.3 illustrate the results for $p_T$ between 0 and 2 GeV, and 2 and 4 GeV, respectively, within the centrality range of 20-30%. For all the $p_T$ range studied the fits converged and were accurate. Additionally, Figure 5.1 displays the reconstruction for $p_T$ ranging from 0 to 20 GeV within the same centrality range. These results allow for the measurement of the $v_2$ coefficient through the Event-Plane, shown on Figure 5.4. The measured $v_2$ exhibits a discernible trend; first, we observe a nearly linear rise in $v_2$ up to a $p_T$ treshold of approximately 1 GeV. Then, we notice a local maximum around 2.5 GeV. At high $p_T$ the Event Plane Method becomes unreliable, resulting in drastic jump in the measured $v_2$.

The same figures are shown for a centrality range of 40-50% in the Appendix A, with the associated $v_2$.

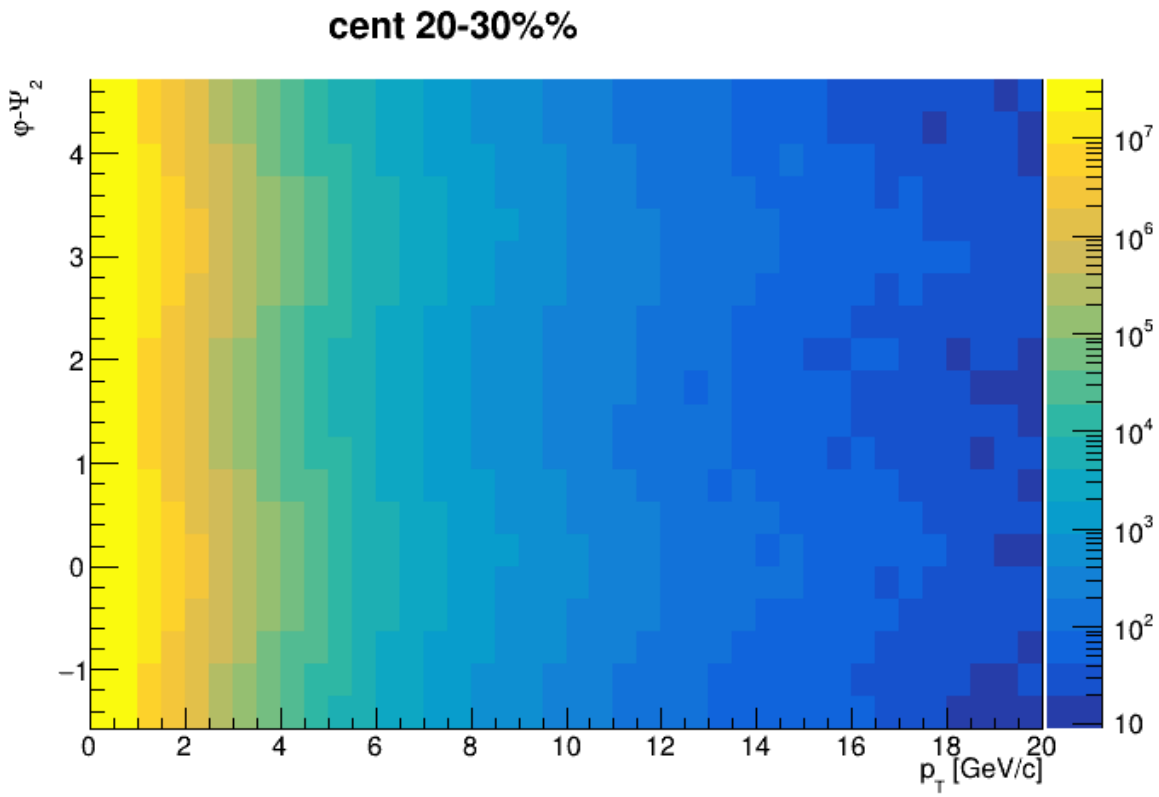


**Figure 5.1:** Reconstruction of $\varphi - \Psi_2$ vs $p_T$ for the centrality range 20-30%.

## 5.2 $v_2$ coefficients through the cumulant methods

We present the elliptic flow $v_2$ as a function of $p_{\mathrm{T}}$ of all charged particles for 20-30% and 40-50% collision centrality in [5.5a, 5.5b]. The results reveal a discernible trend in the elliptic flow $v_2$: an approximatively linear increase of $v_2$ up to $p_{\mathrm{T}} \lesssim 1$ GeV/$c$ for all centrality ranges. A maximum of $v_2$ is reached at around 3.0 GeV/$c$ where a saturation effect becomes apparent. Moreover, as we move toward less central collisions the maximum value of $v_2$ increases. In order to give a better idea of the validity of our results, we present a comparison with published data from ALICE [4].

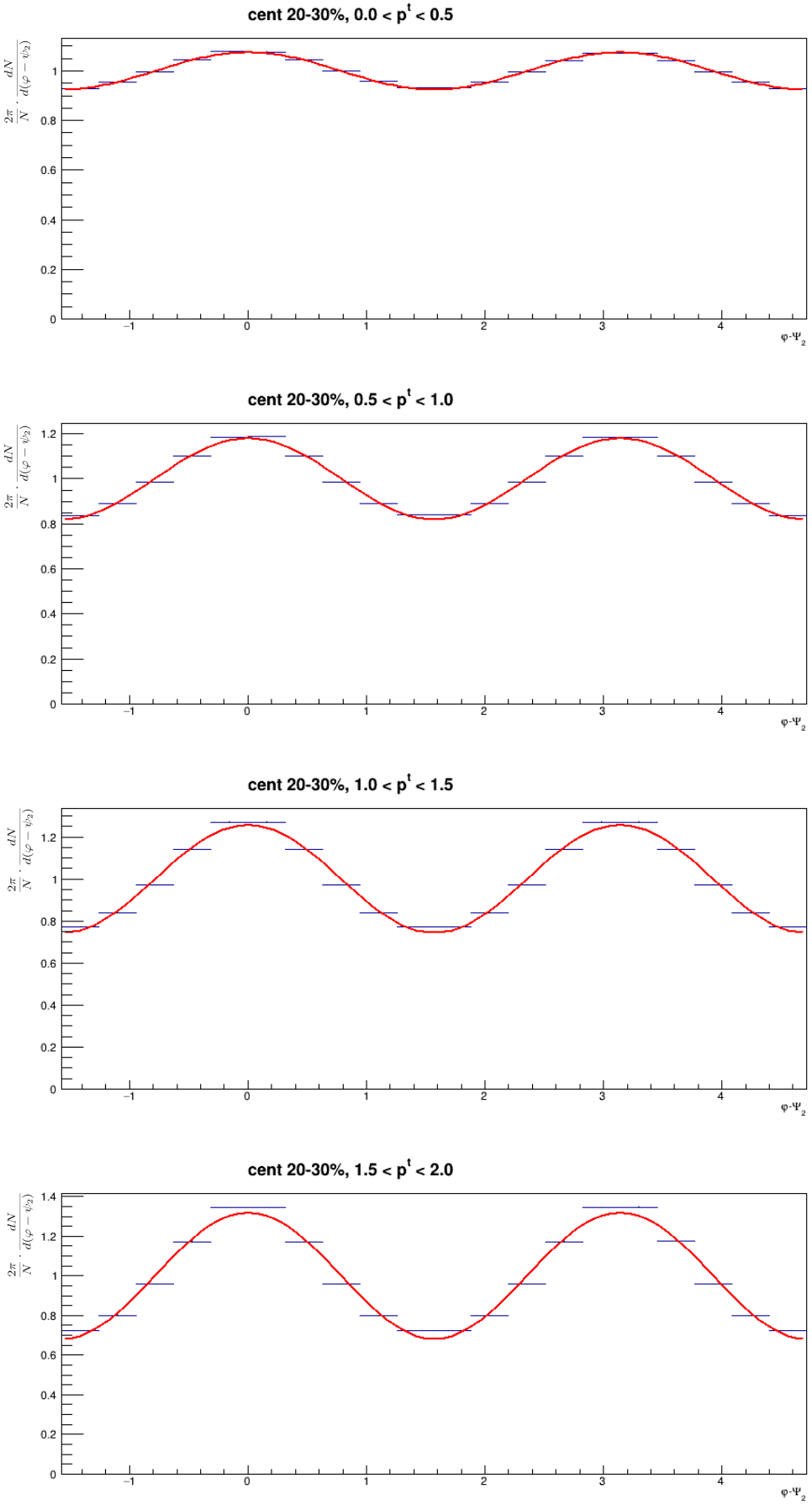


**Figure 5.2:** The azimuthal distribution relative to $\varphi - \Psi_2$ for the centrality range 20-30% for $p_{\mathrm{T}}$ between 0 and 2 GeV.

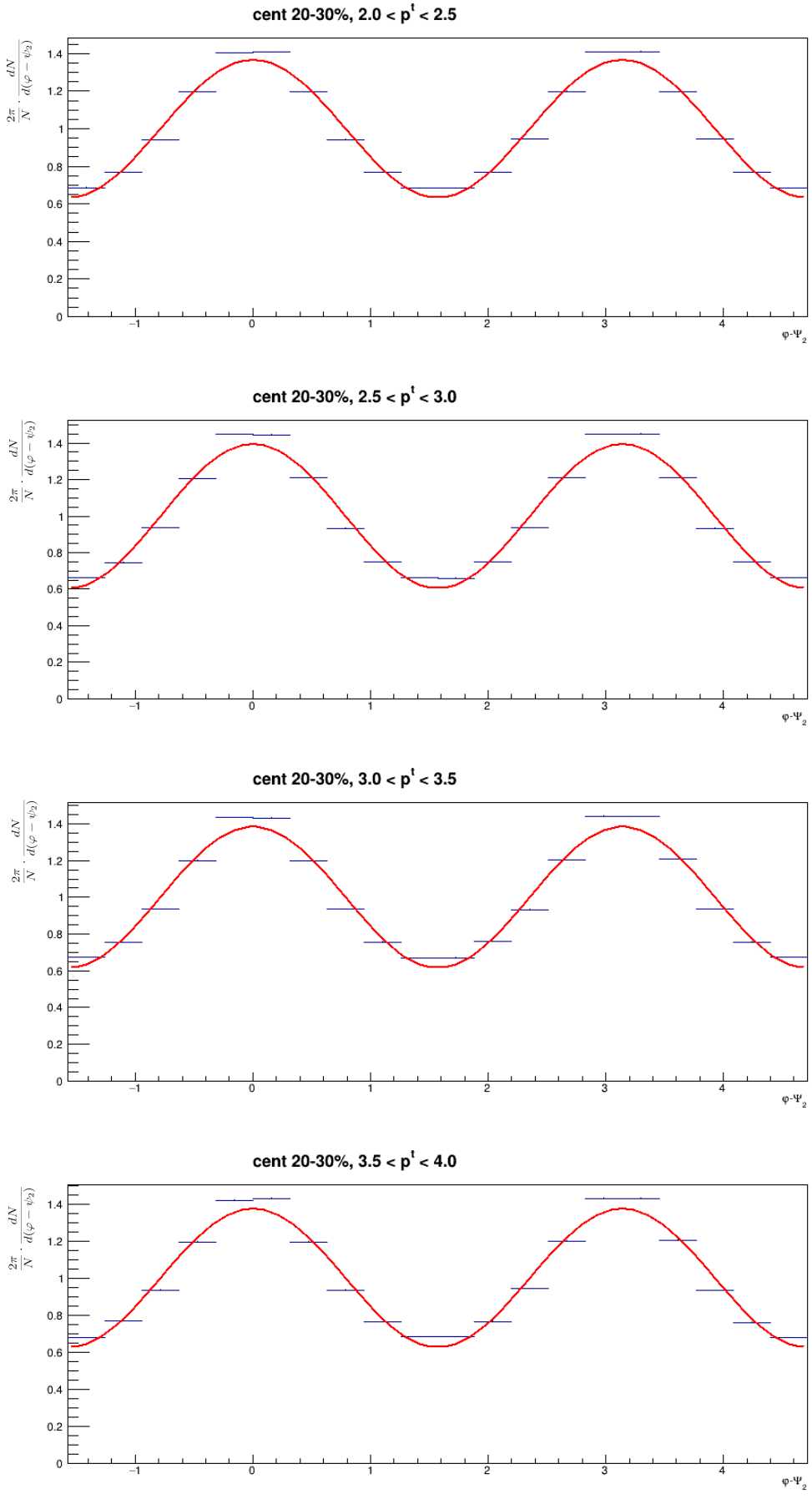


**Figure 5.3:** The azimuthal distribution relative to $\varphi - \Psi_2$ for the centrality range 20-30% for $p_{\mathrm{T}}$ between 2 and 4 GeV.

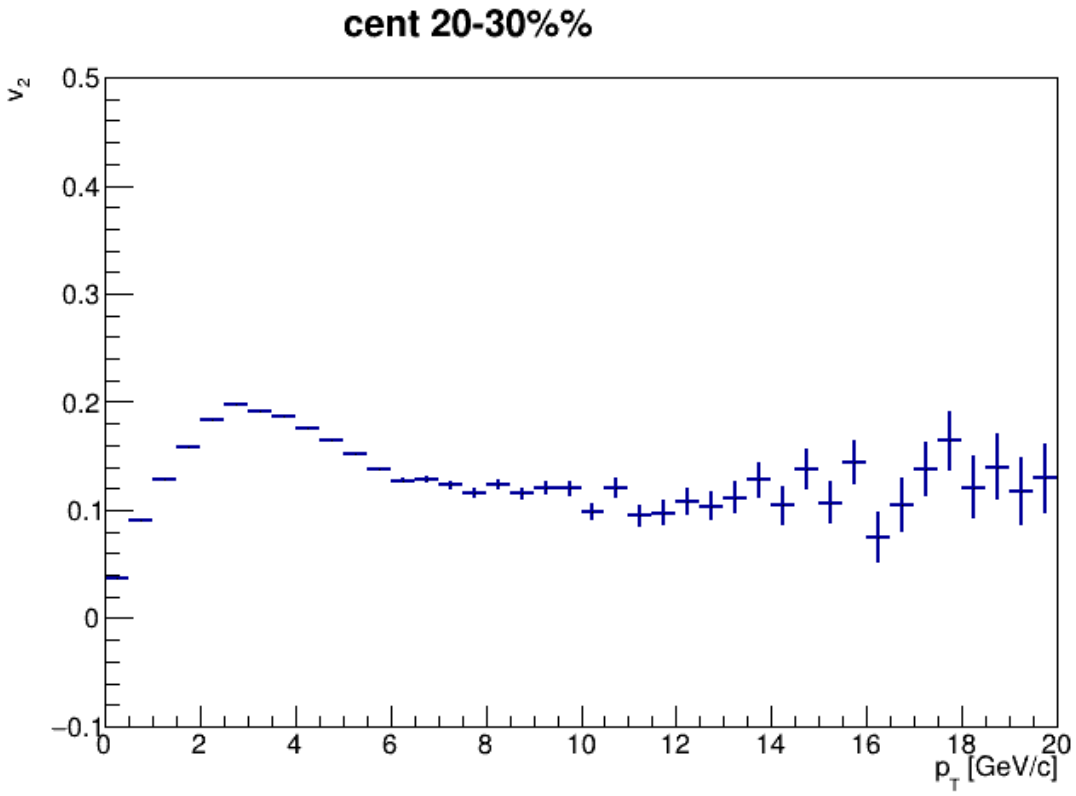


**Figure 5.4:** Reconstruction of $v_2$ vs $p_{\mathrm{T}}$ for the centrality range 20-30%.

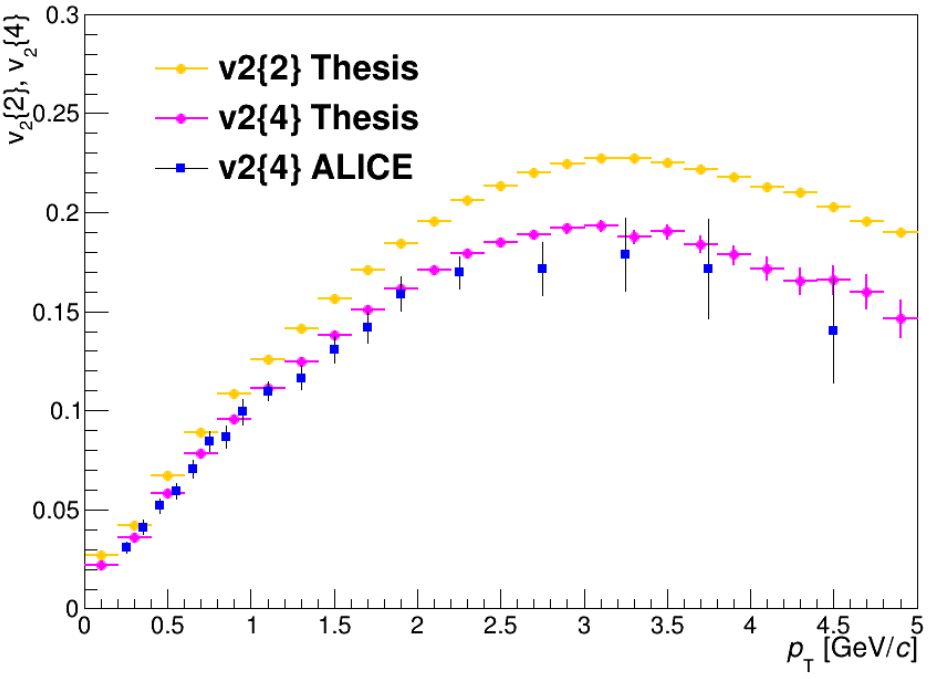


**(a)** Combined $v_2$ as a function of $p_T$ for 20-30% collision centrality through the cumulant method.

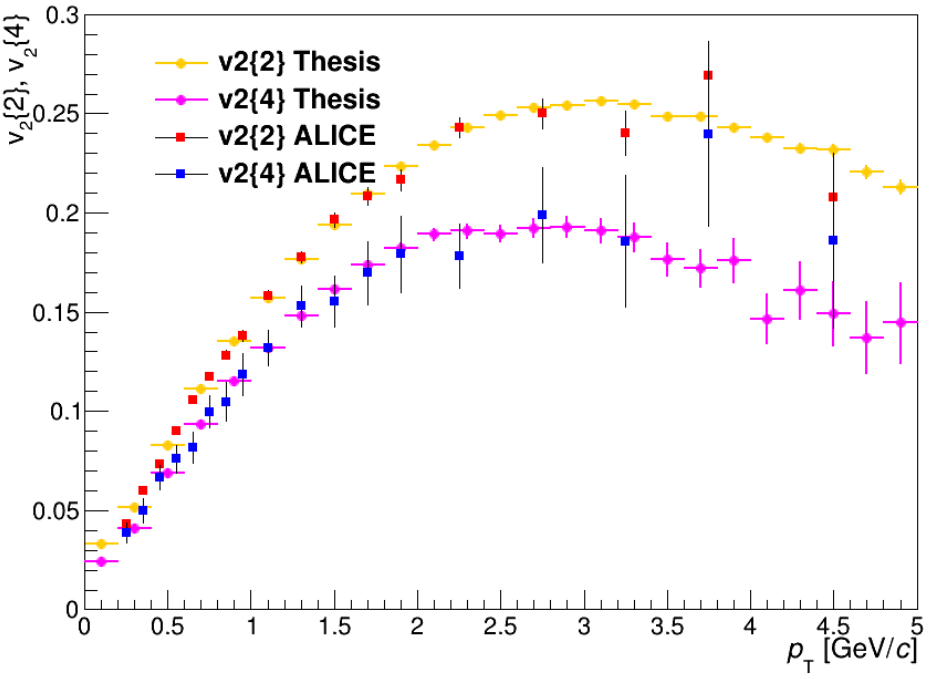


**(b)** Combined $v_2$ as a function of $p_T$ for 40-50% collision centrality.

**Figure 5.5:** Combined $v_2$ for different collision centralities using the cumulant method.

## 5.3 Picking up flow from underlying events

As illustrated in Figure 5.4, a substantial $v_2$ is calculated even at high $p_{\mathrm{T}}$, $p_{\mathrm{T}} > 5GeV/c$, in Pb-Pb collisions. This phenomenon is not attributed to flow but rather to jet quenching, stemming from the shorter (longer) average path length of jets in (out) of the plane, along (perpendicular to) $\Psi_2$. A noteworthy observation in $pp$ collisions is the absence of observed jet quenching thus far. Nevertheless, flow can still influence jet measurements, as defining a jet cone around a high $p_{\mathrm{T}}$ particle captures non-jet particles from the underlying events, with a preference for those in the plane. This was a problem for ATLAS in a recent measurement [3]. Here we want to use it as a way to test if there is flow in a $pp$ collision. The goal is in particular to see if this method can be made sensitive in very low multiplicity collisions.

Figure 5.12 shows that by going to $|\Delta\eta| > 1.3$ we can indeed remove the long-range correlations on the near side, meaning that even for $|\Delta\eta| < 1.3$ the correlations are not due to flow but rather jet correlations.

One challenge with the method arises from the limited $\eta$ acceptance of ALICE ($|\eta| < 0.8$), leading to a rapid depletion of statistics. For instance, for $|\Delta\eta| > 1.3$, we are constrained to accept triggers with $|\eta| > 0.5$, and even then, the acceptance for long-range correlations becomes significantly limited. To mitigate this issue, and after confirming the absence of flow, the following approach is employed:

We establish the non-flow baseline by examining correlations without the jet $p_{\mathrm{T}}$ cut. Then, we analyze the relative changes in correlations relative to this baseline. It is essential to note that both the baseline and variations are normalized to ensure consistent integrals. The results are presented for $|\Delta\eta| = 0.9, 1.1$ and $1.2$ in Figure 5.6. We observe that the sharpest relative changes are obtained for $|\Delta\eta| = 0.9$, while the bump around $\Delta\varphi = 0$ flattens out for $|\Delta\eta| = 1.1$ and almost disappears for $|\Delta\eta| = 1.2$.

After confirming the feasibility of utilizing $|\Delta\eta| > 0.9$, we proceed to demonstrate the presence of flow and antiflow correlations, as depicted in Figure 5.7. To give a comparison we also present the absence of flow and antiflow correlations in Figure 5.8. Analogous results for $|\Delta\eta| > 1.1$ and $|\Delta\eta| > 1.2$ can be found in the appendix.

Subsequently, our focus shifts to examining the multiplicity dependence, with the corresponding results showcased in Figures 5.9, 5.10, 5.11. Figure 5.9 shows the results for $|\Delta\eta| = 0.9$. Here, the presence of the anti-flow peak around $|\Delta\varphi| = 0$ appears independent of the multiplicity class. Figure 5.10 displays the results for $|\Delta\eta| = 1.1$. Notably, the anti-flow peak around $|\Delta\varphi| = 0$ is most prominent in the multiplicity classes 0-10%, 10-20%, and 30-100%. Figure 5.11 exhibits the results for $|\Delta\eta| = 1.2$. Here, we do not observe the presence of the anti-flow peak around $|\Delta\varphi| = 0$. We speculate that while flow and anti-flow may still be present, limited statistics obscure their detection, given the considerable variation in jet contribution and similar-sized flow contribution.

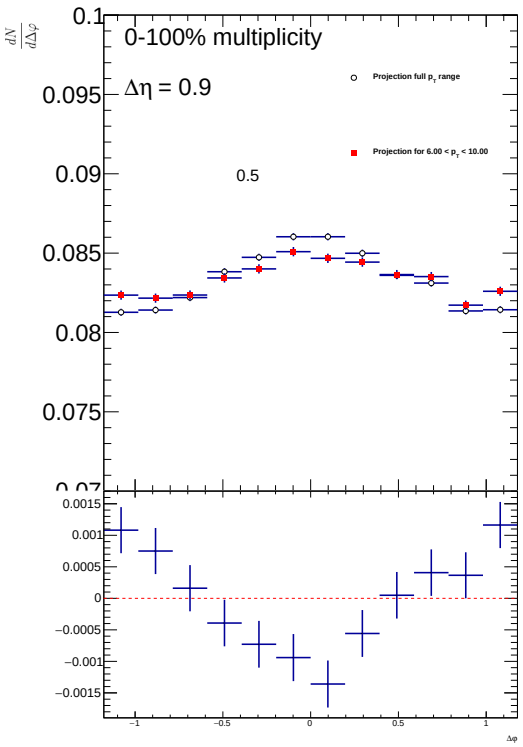


**(a)** The bump around $\varphi = 0$ is clearly visible for $\Delta\eta = 0.9$

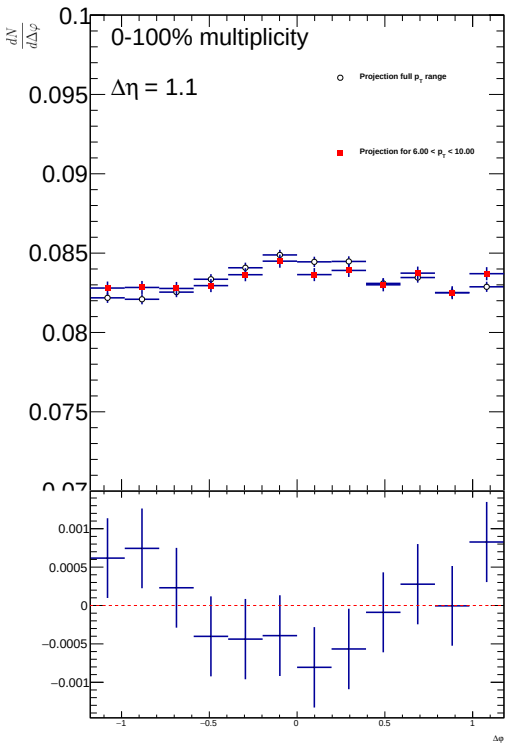


**(b)** The bump around $\varphi = 0$ diminished for $\Delta\eta = 1.1$

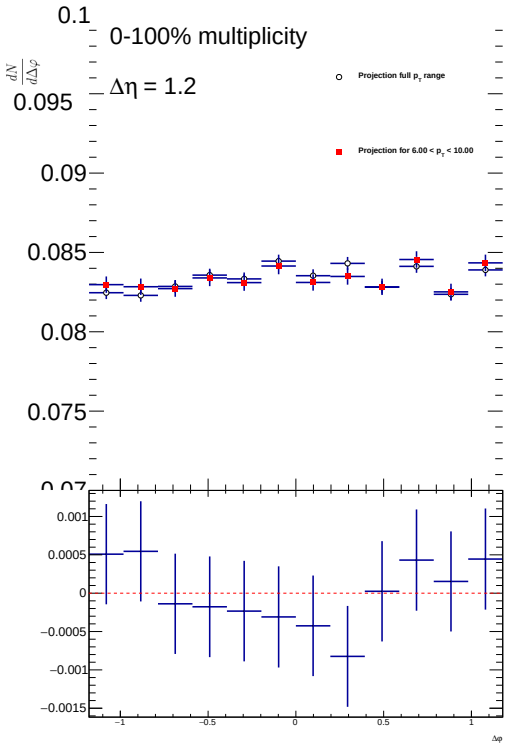


**(c)** The bump around $\varphi = 0$ disappears for $\Delta\eta = 1.2$

**Figure 5.6:** Projected distribution for different $p_{\mathrm{T}}$ bin of $\Delta\varphi$ across the entire $p_{\mathrm{T}}$ range, focusing on the 0-100% multiplicity range, with variations on $\Delta\eta$. The bottom pannel shows the difference between the projections of the full $p_{\mathrm{T}}$ range and a specific bin of interest, here 6 to 10 GeV.

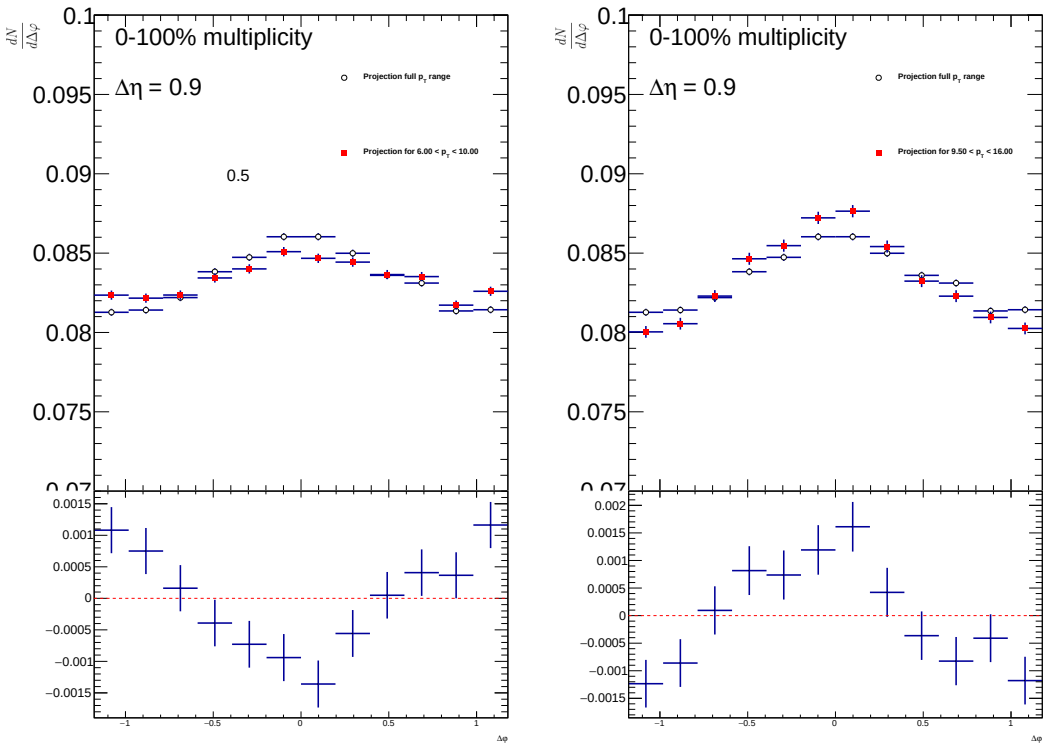


**(a)** The bump around $\varphi = 0$ is clearly visible for $\Delta\eta = 0.9$ for this specific $p_{\mathrm{T}}$ range.

**(b)** The bump around $\varphi = 0$ is inverted for $\Delta\eta = 0.9$ for this specific $p_{\mathrm{T}}$ range.

**Figure 5.7:** Projected distribution for different $p_{\mathrm{T}}$ bin of $\Delta\varphi$ across the entire $p_{\mathrm{T}}$ range, focusing on the 0-100% multiplicity range, with no variations on $\Delta\eta$. The bottom pannel shows the difference between the projections of the full $p_{\mathrm{T}}$ range and specific bins of interest, here 6 to 10 GeV and 9.5 to 16 GeV. The emergence of the anti-flow and flow peaks is evident.

## 5.4 Discussion

The results presented in Chap. 5 have two primary objectives. Firstly, they aim to replicate and compare to published results with our own standard method, across various centrality intervals, a goal successfully achieved for all investigated ranges. It is important to note that the data from ALICE and the aforementionned results from the collaboration were some of the first results and data ever published by the collaboration. However, it is essential to acknowledge a potential overestimation of the coefficient $v_2$ in our method, as we do not account for fluctuations and non-flow effects. Non-flow effects are often characterized by particles originating from resonant decays. Although higher-order correlations such as $v_2\{4\}$ can help mitigate most non-flow correlations, they are still influenced by these fluctuations.

The second objective involves addressing an open question concerning smaller collision systems, such as *pp*. Our aim was to leverage underlying events for analyzing flow-like effects initially observed by the ATLAS collaboration. The approach involved relaxing the asymmetrical cut on $\Delta\eta$ to enhance the precision of flow measurements. While the direct measurement of this flow was not achieved, our observations affirm the presence of flow and anti-flow in these systems. Notably, the emphasis on the trigger particle's lack of flow served as a key aspect of this approach, allowing us to effectively probe the flow originating from the underlying events.

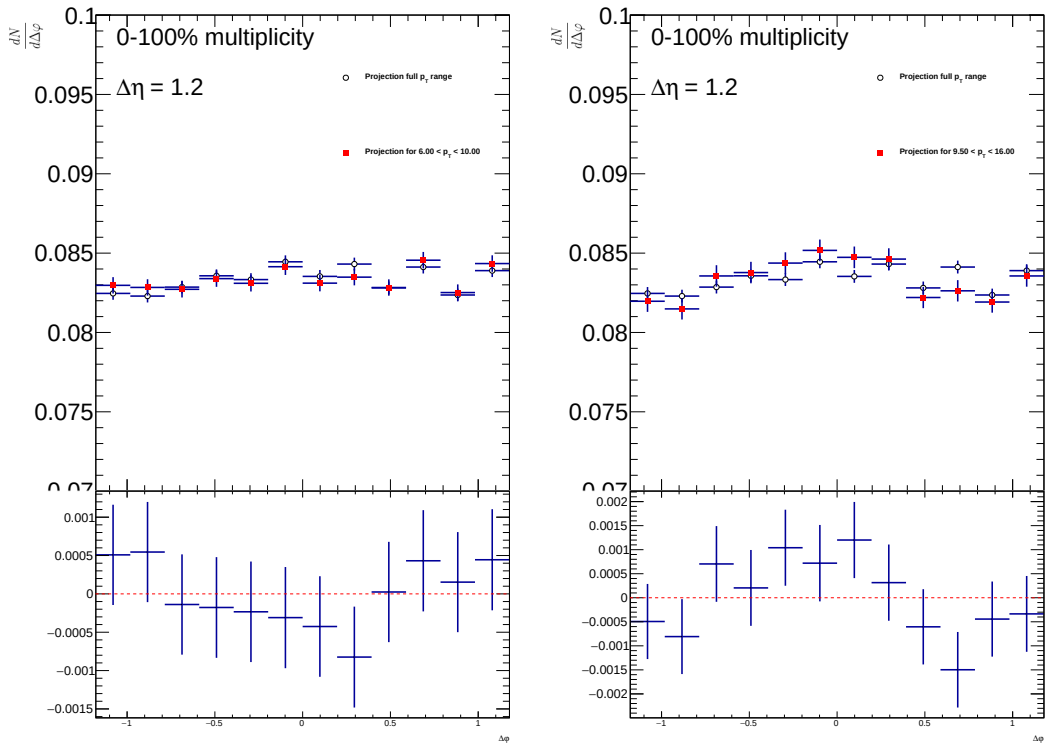


**(a)** The bump around $\varphi = 0$ is clearly visible for $\Delta\eta = 1.2$

**(b)** The bump around $\varphi = 0$ is inverted for $\Delta\eta = 1.2$

**Figure 5.8:** Projected distribution for different $p_{\mathrm{T}}$ bin of $\Delta\varphi$ across the entire $p_{\mathrm{T}}$ range, focusing on the 0-100% multiplicity range, with no variations on $\Delta\eta$. The bottom pannel shows the difference between the projections of the full $p_{\mathrm{T}}$ range and specific bins of interest, here 6 to 10 GeV and 9.5 to 16 GeV. The emergence of the anti-flow and flow peaks is evident albeit smaller.

In conclusion, we successfully reproduced results published by the ALICE collaboration using the most common method of flow analysis. Additionally, we successfully devised and implemented a novel method to detect flow signals from low-multiplicity *pp* collisions. As an outlook, it may be of great interest to quantify these flow signals to gain a better understanding of small systems.

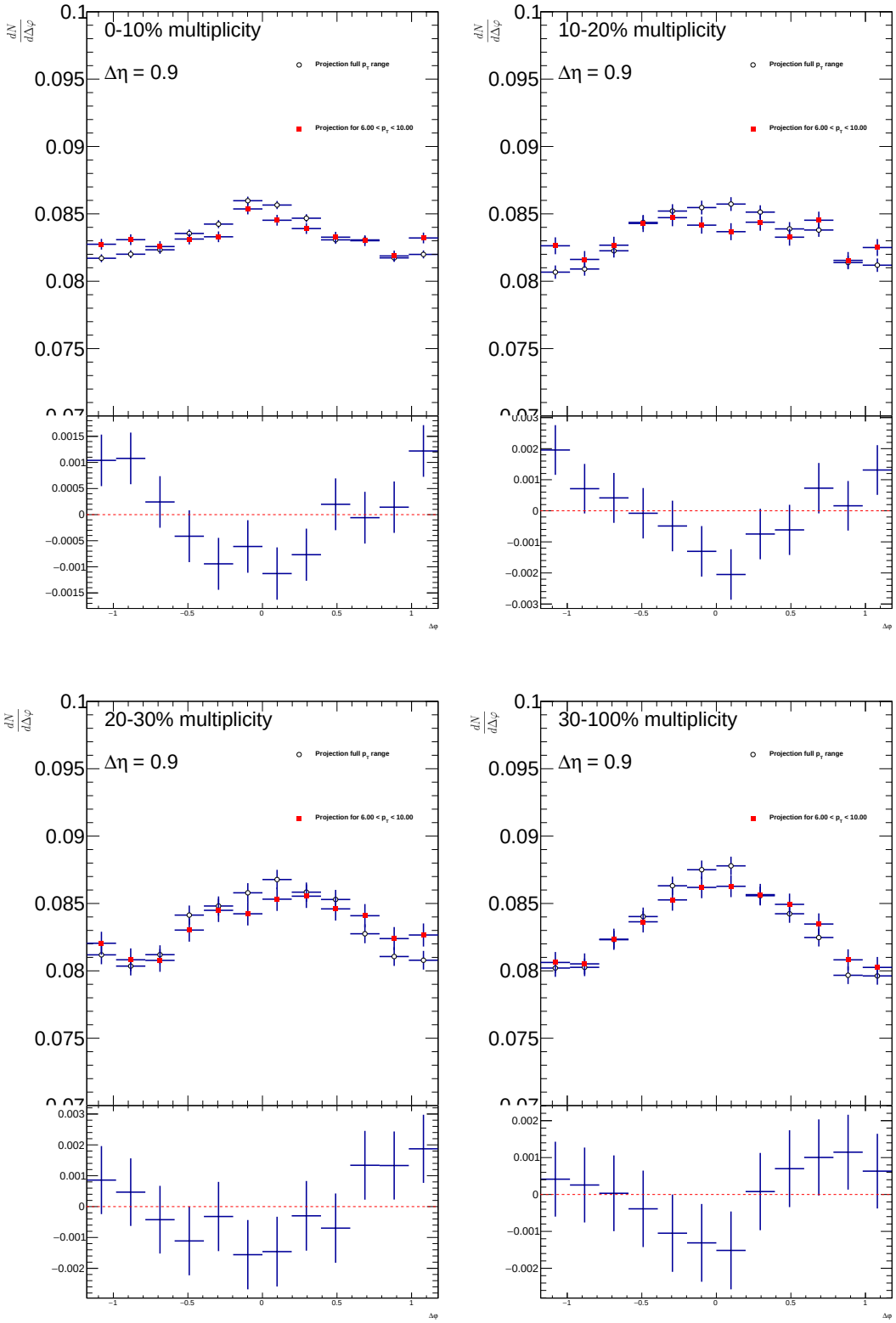


**Figure 5.9:** Projected distribution for different $p_{\mathrm{T}}$ bin of $\Delta\varphi$ across the entire $p_{\mathrm{T}}$ range, for different multiplicities, with no variations on $\Delta\eta$. The bottom pannel shows the difference between the projections of the full $p_{\mathrm{T}}$ range and specific bins of interest, here 6 to 10 GeV.

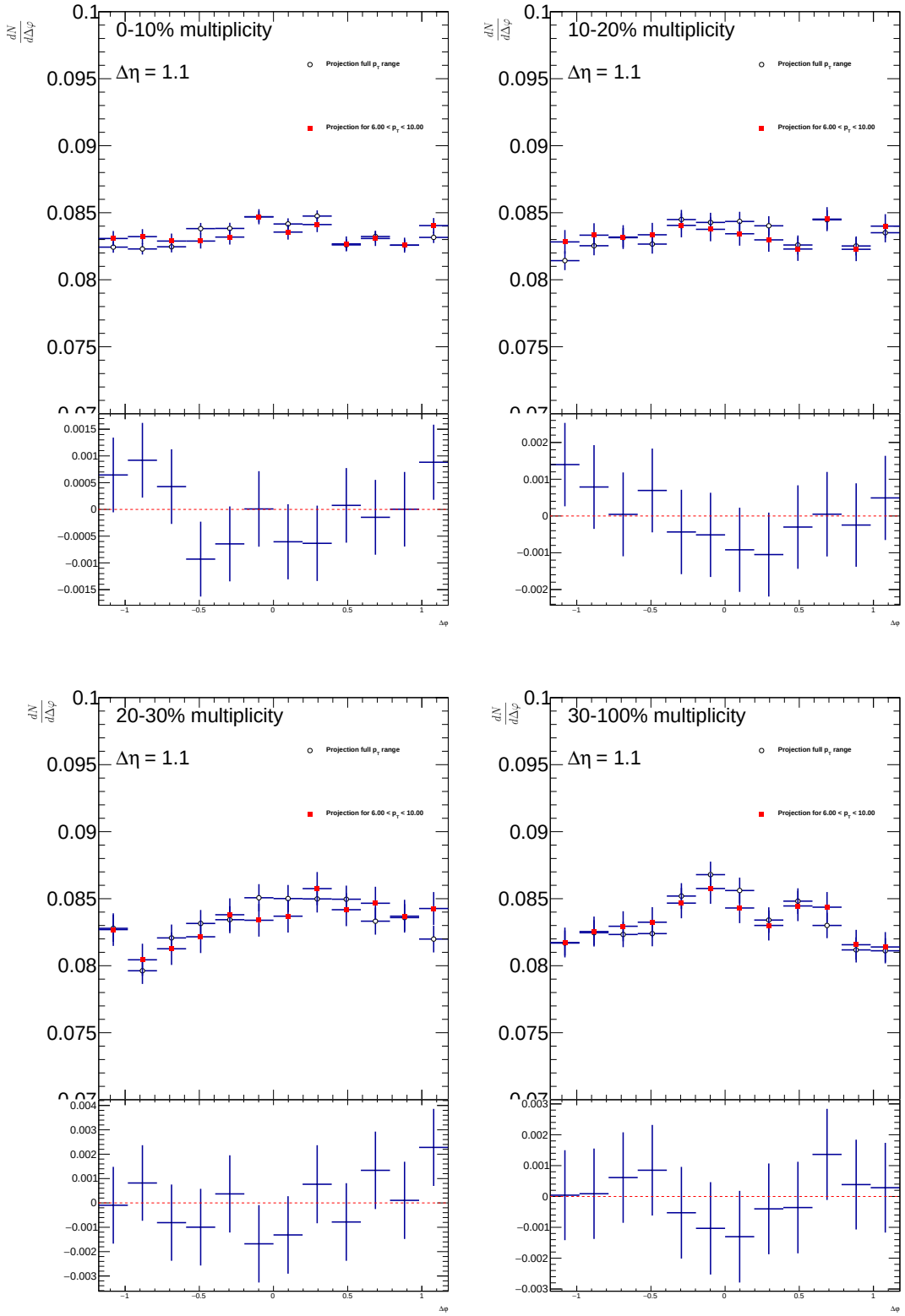


**Figure 5.10:** Projected distribution for different $p_{\mathrm{T}}$ bin of $\Delta\varphi$ across the entire $p_{\mathrm{T}}$ range, for different multiplicities, with no variations on $\Delta\eta$. The bottom pannel shows the difference between the projections of the full $p_{\mathrm{T}}$ range and specific bins of interest, here 6 to 10 GeV.

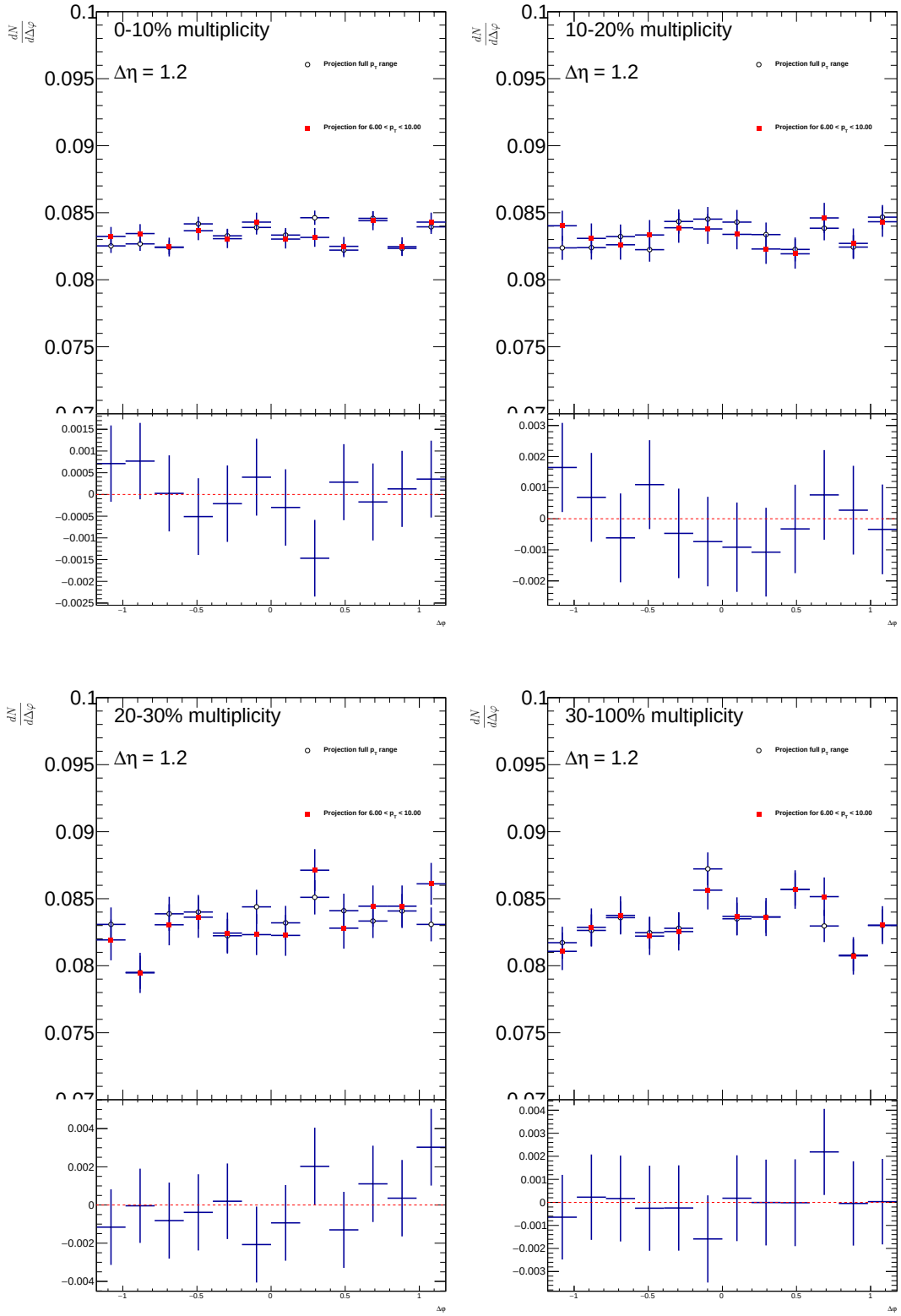


**Figure 5.11:** Projected distribution for different $p_{\mathrm{T}}$ bin of $\Delta\varphi$ across the entire $p_{\mathrm{T}}$ range, for different multiplicities, with no variations on $\Delta\eta$.

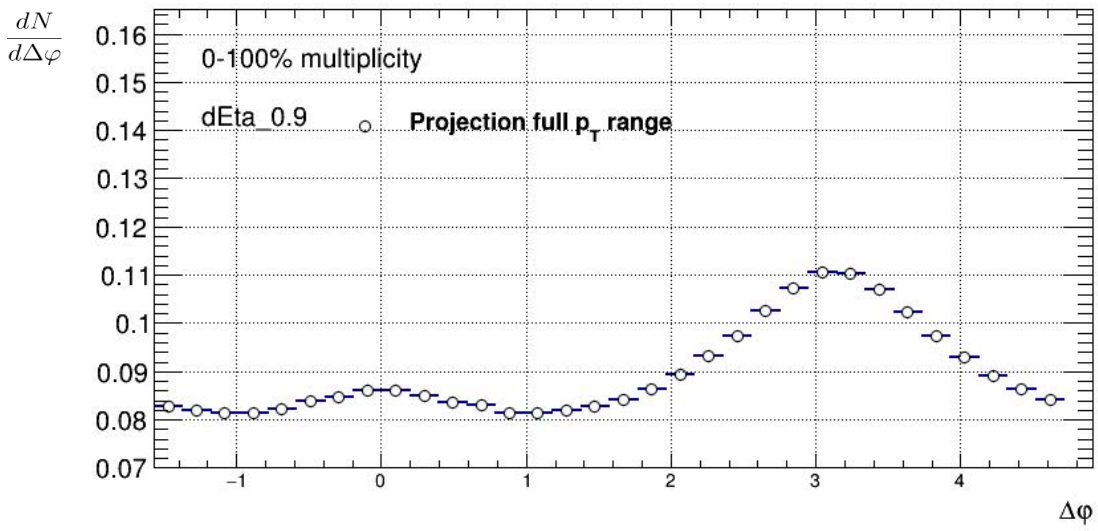


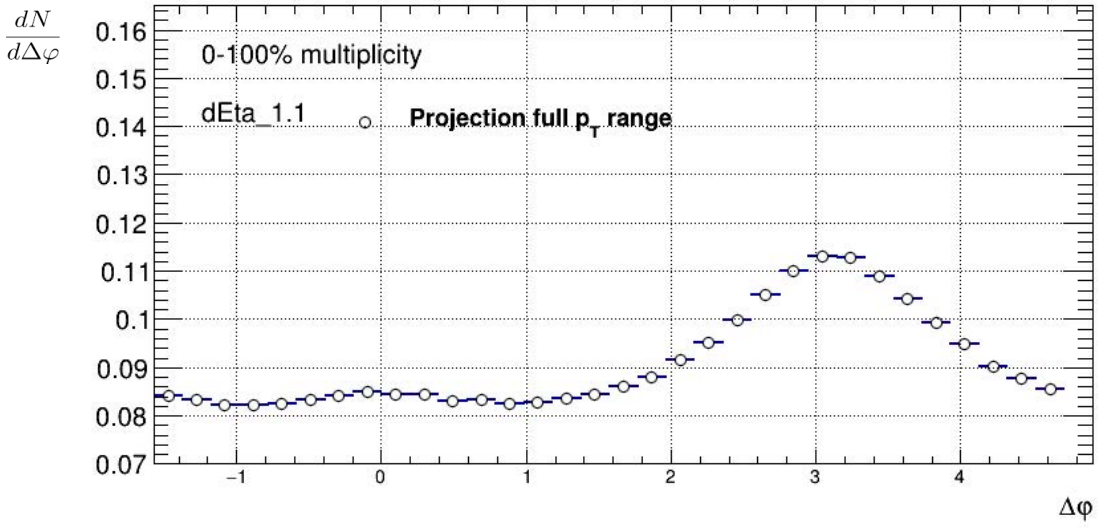


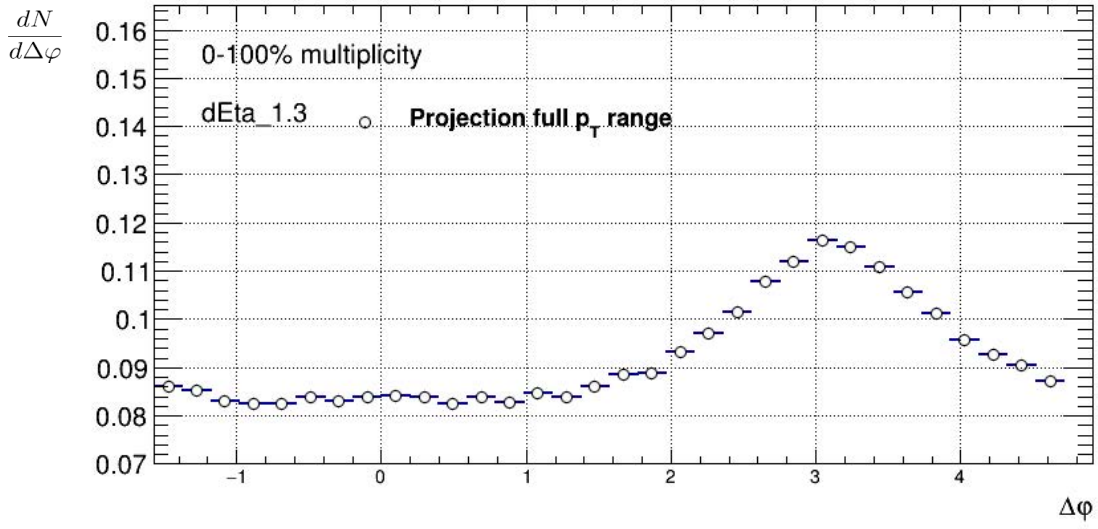


**Figure 5.12:** Projection of $\Delta\varphi$ for the full $p_{\mathrm{T}}$ range for 100% centrality for different value of $\Delta\eta$.

# Bibliography


[1] S. Chatrchyan et al. (CMS Collaboration). "Centrality dependence of dihadron correlations and azimuthal anisotropy harmonics in PbPb collisions at $\sqrt{s_{\mathrm{NN}}} = 2.76\,\mathrm{TeV}$ ". In: *The European Physical Journal* C 72 (2012). DOI: 10.1140/epjc/s10052-012-2012-3.

[2] V. Khachatryan et al. (CMS Collaboration). "Observation of long-range, near-side angular correlations in proton-proton collisions at the LHC." In: *Journal of High Energy Physics* 09 (2010). DOI: 10.1007/jhep09(2010)091.

[3] G. Aad and all. "Observation of Long-Range Elliptic Azimuthal Anisotropies in heavy ion Collisions with the ATLAS Detector". In: *Physical Review Letters* 116.17 (Apr. 2016). ISSN: 1079-7114. DOI: 10.1103/physrevlett.116.172301. URL: http://dx.doi.org/10.1103/PhysRevLett.116.172301.

[4] Aamodt. "Elliptic Flow of Charged Particles in Pb-Pb Collisions". In: *Physical Review Letters* 105.25 (Dec. 2010). ISSN: 1079-7114. DOI: 10.1103/physrevlett.105.252302. URL: http://dx.doi.org/10.1103/PhysRevLett.105.252302.

[5] J. Adams and al. "Experimental and theoretical challenges in the search for the quark–gluon plasma: The STAR Collaboration's critical assessment of the evidence from RHIC collisions". In: *Nuclear Physics A* 757.1 (2005). First Three Years of Operation of RHIC, pp. 102–183. ISSN: 0375-9474. DOI: https://doi.org/10.1016/j.nuclphysa.2005.03.085. URL: https://www.sciencedirect.com/science/article/pii/S0375947405005294.

[6] Madan M. Aggarwal. "Elliptic Flow in Relativistic Heavy-Ion Collisions". In: *Advances in Nuclear Physics*. Ed. by Rajeev K. Puri et al. Singapore: Springer Singapore, 2021, pp. 161–188. ISBN: 978-981-15-9062-7.

[7] D.J. Gross et al. "Ultraviolet Behavior of Non-Abelian Gauge Theories". In: *Physical Review Letters* 30 (1977). DOI: 10.1103/PhysRevLett.30.1343.

[8] J.C. Collins et al. "Superdense Matter: Neutrons or Asymptotically Free Quarks?" In: *Physical Review Letters* 34 (1975). DOI: 10.1103/PhysRevLett.34.1353.

[9] N. Cabibbo et al. "Exponential hadronic spectrum and quark liberation". In: *Physics Letters* B 59 (1975). DOI: 10.1016/0370-2693(75)90158-6.

[10] I. Arsene and al. "Quark–gluon plasma and color glass condensate at RHIC? The perspective from the BRAHMS experiment". In: *Nuclear Physics A* 757.1 (2005). First Three Years of Operation of RHIC, pp. 1–27. ISSN: 0375-9474. DOI: https://doi.org/10.1016/j.nuclphysa.2005.02.130. URL: https://www.sciencedirect.com/science/article/pii/S0375947405002770.

[11] Ante Bilandzic, Raimond Snellings and Sergei Voloshin. "Flow analysis with cumulants: Direct calculations". In: *Physical Review C* 83.4 (Apr. 2011). ISSN: 1089-490X. DOI: 10.1103/physrevc.83.044913. URL: http://dx.doi.org/10.1103/PhysRevC.83.044913.

[12] Ante Bilandzic, Raimond Snellings and Sergei Voloshin. "Flow analysis with cumulants: Direct calculations". In: *Physical Review C* 83.4 (Apr. 2011). ISSN: 1089-490X. DOI: 10.1103/physrevc.83.044913. URL: http://dx.doi.org/10.1103/PhysRevC.83.044913.

[13] Nicolas Borghini, Phuong Mai Dinh and Jean-Yves Ollitrault. "New method for measuring azimuthal distributions in nucleus-nucleus collisions". In: *Physical Review C* 63.5 (Apr. 2001). ISSN: 1089-490X. DOI: 10.1103/physrevc.63.054906. URL: http://dx.doi.org/10.1103/PhysRevC.63.054906.

[14] CERN. *CERN Annual report 2020*. 2021. DOI: 10.17181/AnnualReport2020.

[15] ALICE Collaboration. "ALICE forward detectors: FMD, TO and V0. Technical Design report". In: (2004). URL: https://cds.cern.ch/record/781854.

[16] Particle Data Group. "Review of Particle Physics". In: *Progress of Theoretical and Experimental Physics* (2020). DOI: 10.1093/ptep/ptaa104.

[17] U. Heinz. "Early Collective Expansion: Relativistic Hydrodynamics and the Transport Properties of QCD Matter". In: *Relativistic Heavy Ion Physics* (2010). DOI: 10.1007/978-3-642-01539-7_9.

[18] Ulrich Heinz and Maurice Jacob. *Evidence for a New State of Matter: An Assessment of the Results from the CERN Lead Beam Programme*. 2000. arXiv: nucl-th/0002042 [nucl-th].

[19] Aleksi Kurkela et al. "Effective kinetic description of event-by-event pre-equilibrium dynamics in high-energy heavy-ion collisions". In: *Phys. Rev. C* 99 (3 Mar. 2019), p. 034910. DOI: 10.1103/PhysRevC.99.034910. URL: https://link.aps.org/doi/10.1103/PhysRevC.99.034910.

[20] H.D. Politzer. "Reliable Perturbative Results for Strong Interactions?" In: *Physical Review Letters* 30 (1973). DOI: 10.1103/PhysRevLett.30.1346.

[21] F. Rademakers R. Brun. "ROOT - An object oriented data analysis framework". In: *Nuclear Instruments and Method in Physics* (1997).

[22] Johann Rafelski and Berndt Müller. "Strangeness Production in the Quark-Gluon Plasma". In: *Phys. Rev. Lett.* 48 (16 Apr. 1982), pp. 1066–1069. DOI: 10.1103/PhysRevLett.48.1066. URL: https://link.aps.org/doi/10.1103/PhysRevLett.48.1066.

[23] E.V. Shuryak. "Quark-gluon plasma and hadronic production of leptonsm photons and psions". In: *Physics Letters* B 78 (1978). DOI: 10.1016/0370-2693(78)90370-2.

# Appendix A

# Event-Plan and flow measurements

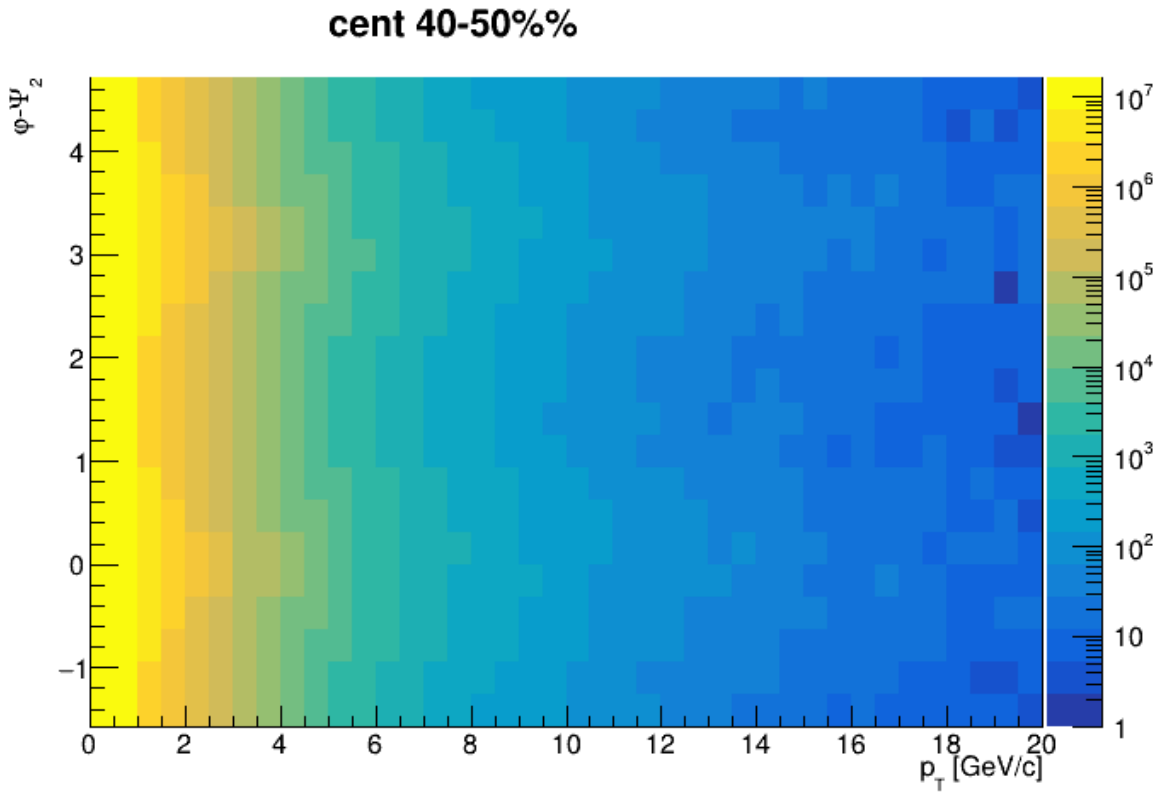


**Figure A.1:** Reconstruction of $\varphi - \Psi_2$ vs $p_{\mathrm{T}}$ for the centrality range 40-50%.

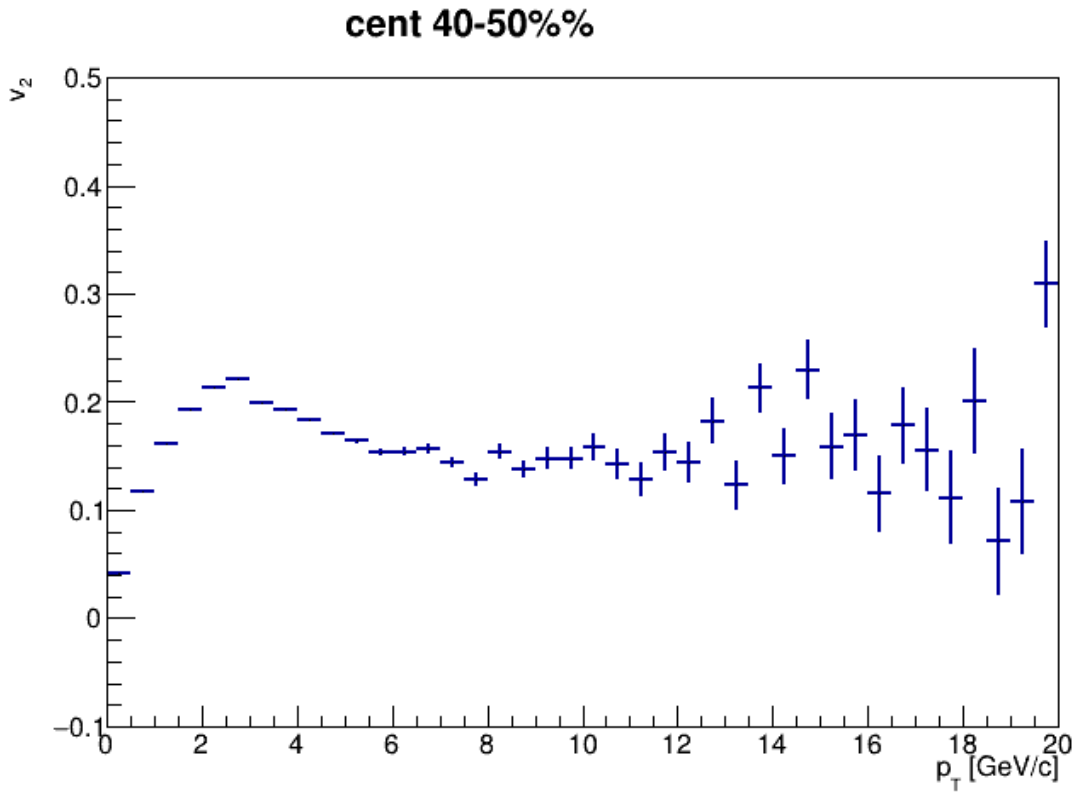


**Figure A.2:** Reconstruction of $v_2$ vs $p_{\mathrm{T}}$ for the centrality range 40-50%.

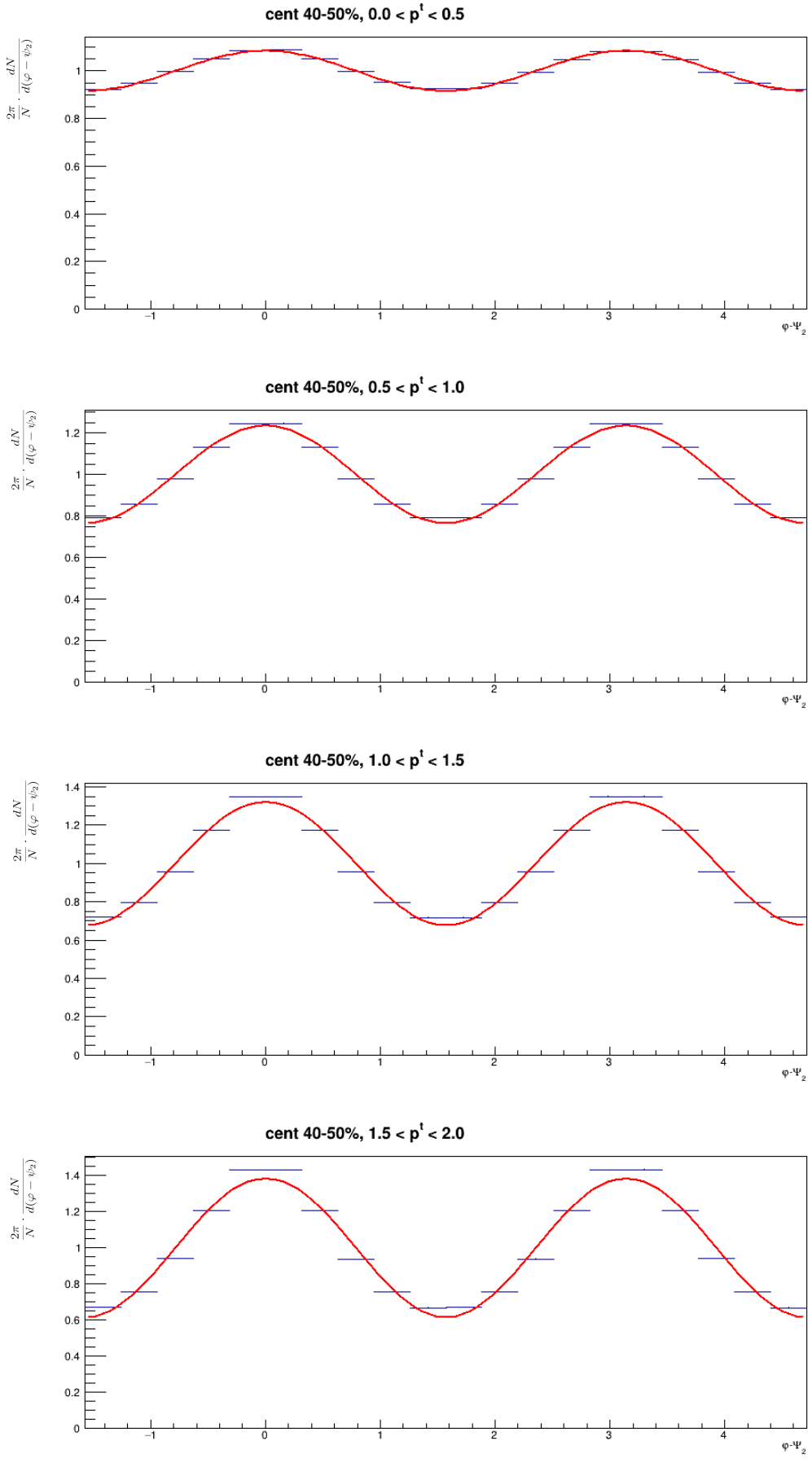


**Figure A.3:** The azimuthal distribution relative to $\varphi - \Psi_2$ for the centrality range 40-50% for $p_{\mathrm{T}}$ between 0 and 2 GeV.

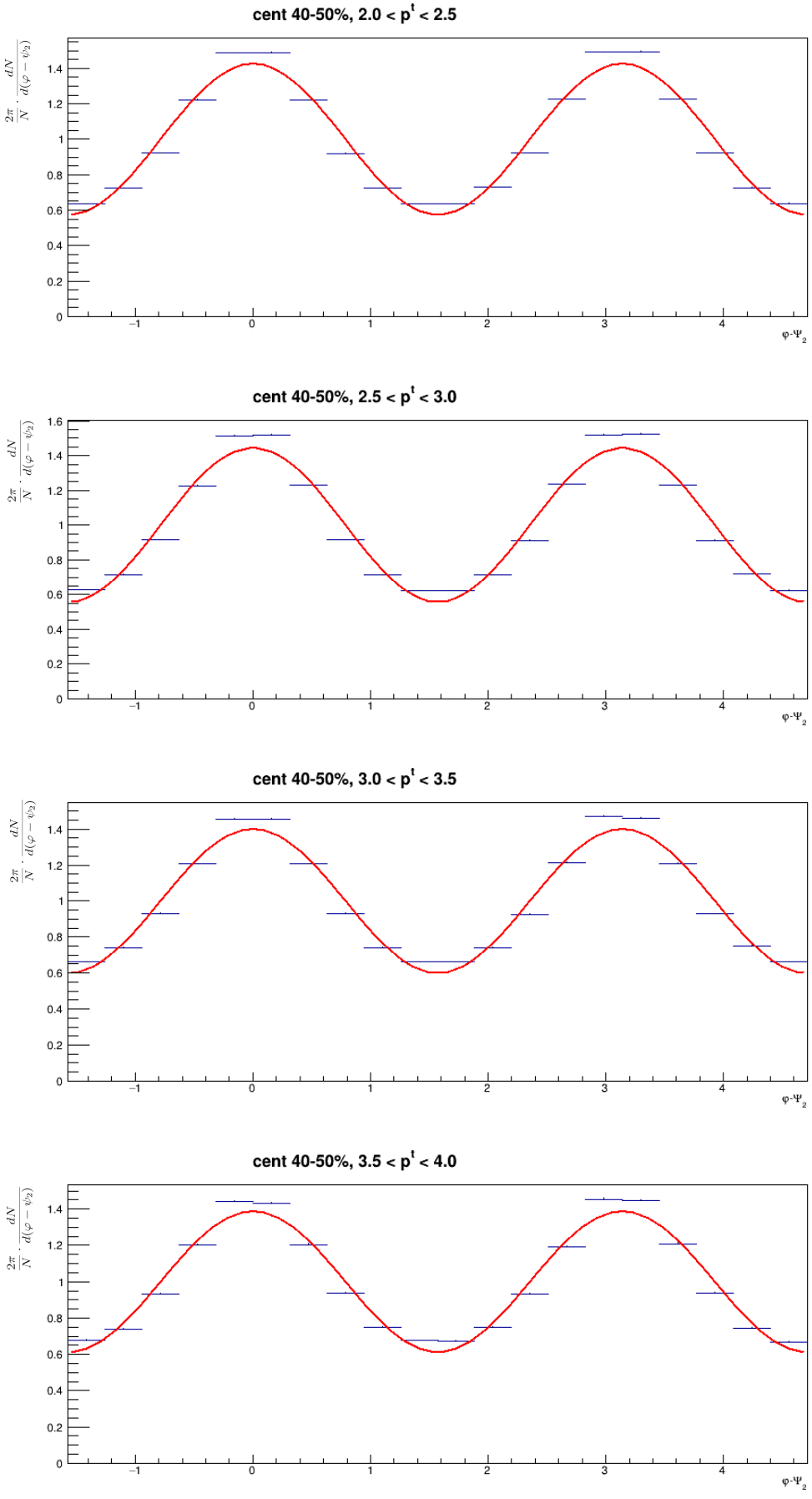


**Figure A.4:** The azimuthal distribution relative to $\varphi - \Psi_2$ for the centrality range 40-50% for $p_{\mathrm{T}}$ between 2 and 4 GeV.

# Appendix B

# Flow from underlying events - an extensive view of the results

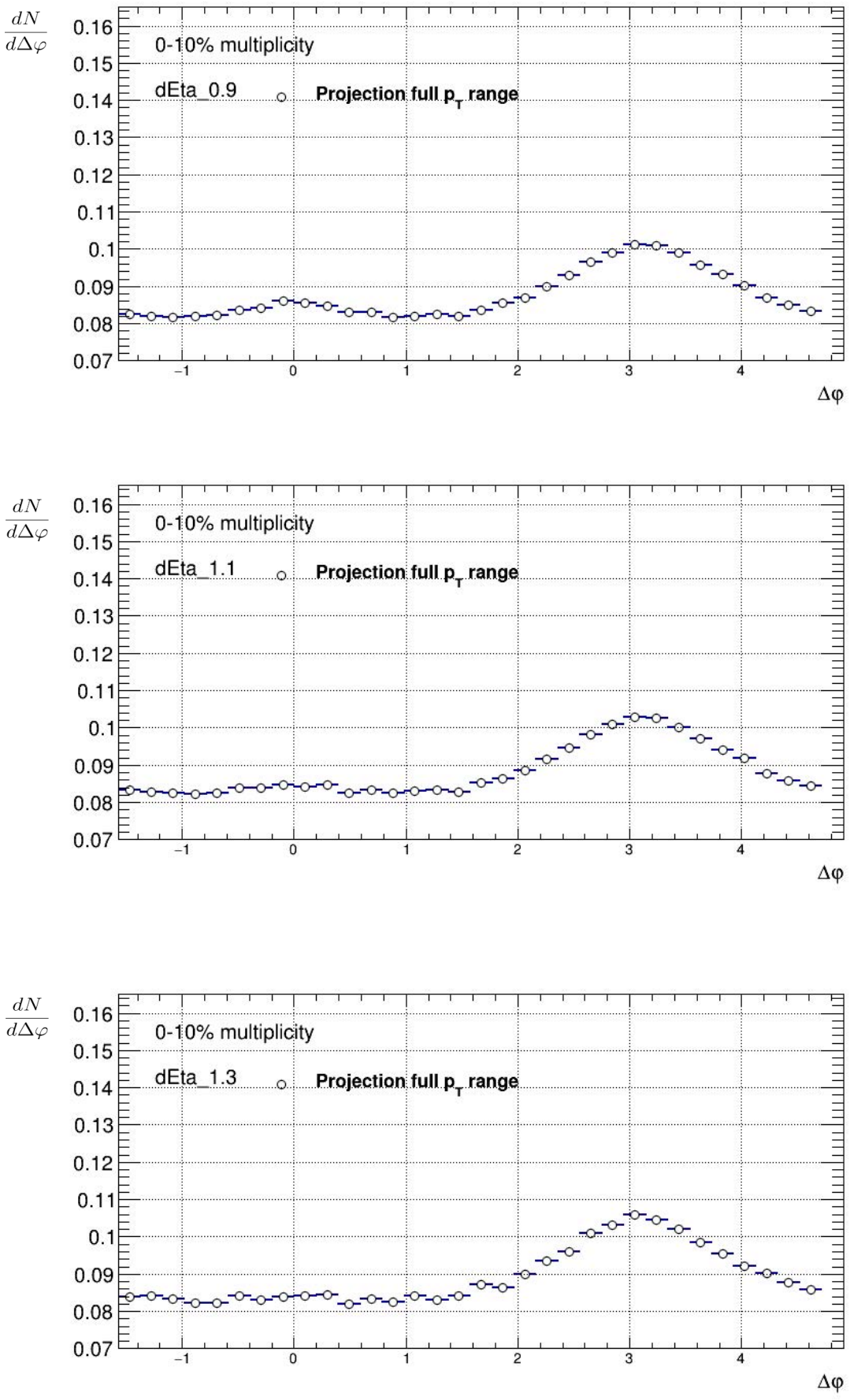


**Figure B.1:** Projection of $\Delta\varphi$ for the full $p_{\mathrm{T}}$ range for 0-10% multiplicity for different value of $\Delta\eta$.

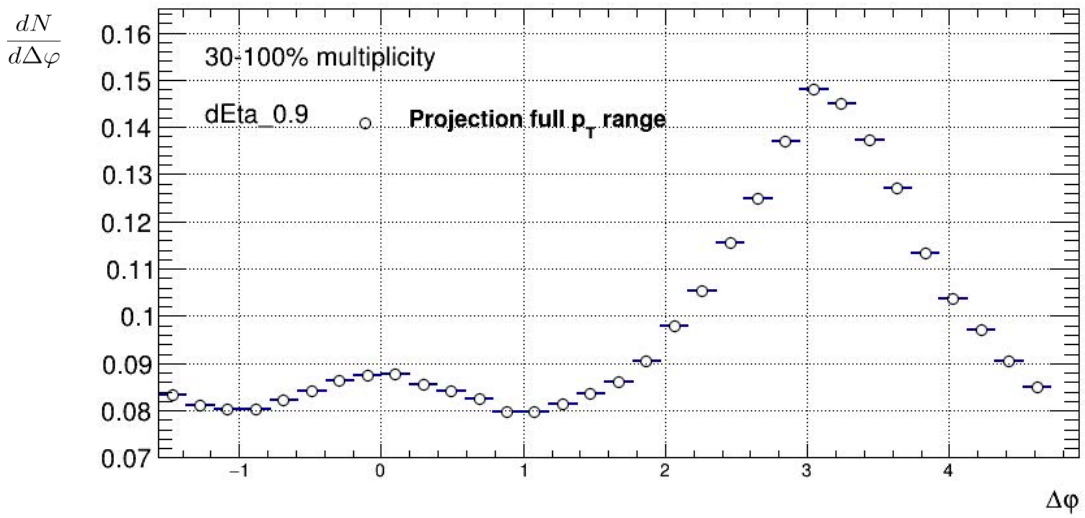


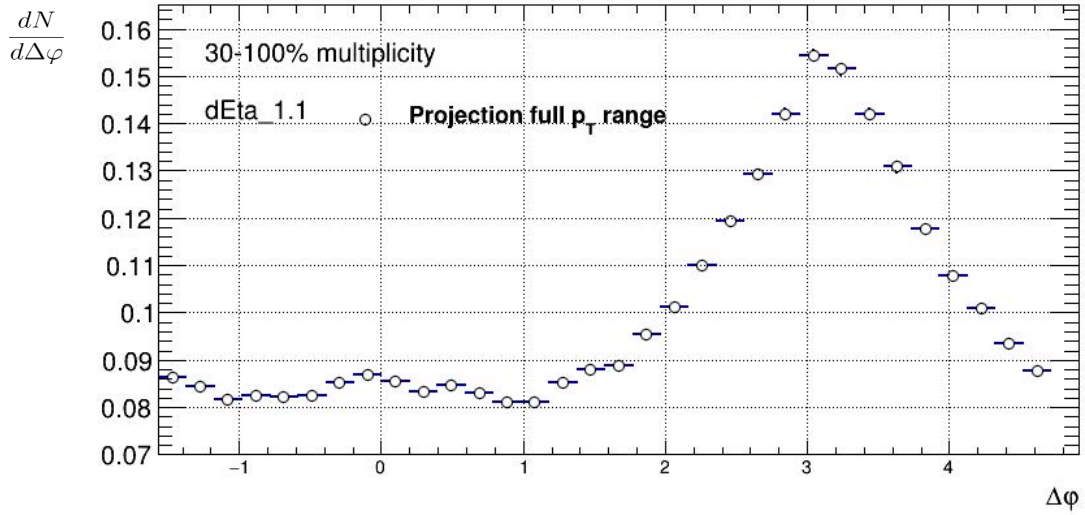


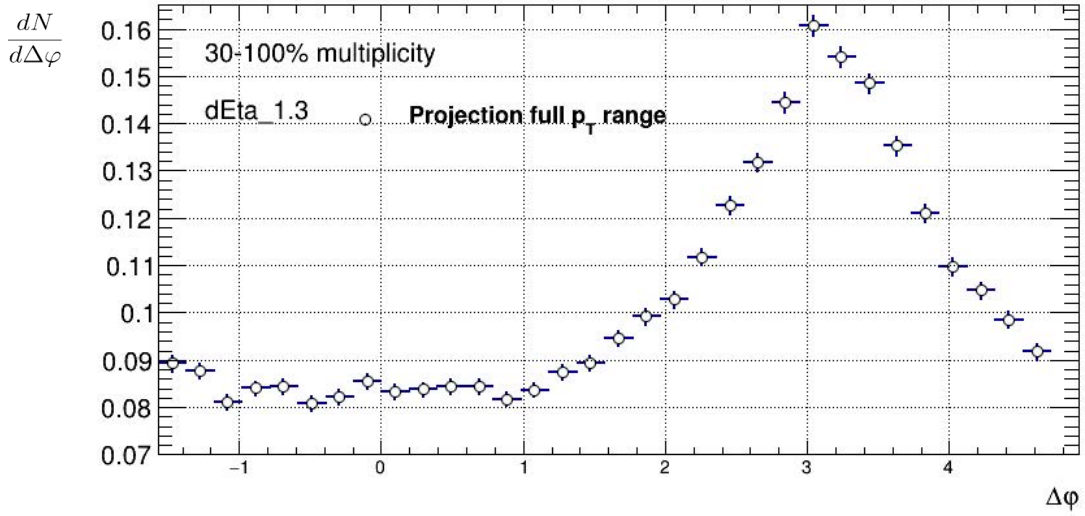


**Figure B.2:** Projection of $\Delta\varphi$ for the full $p_{\mathrm{T}}$ range for 30-100% multiplicity for different value of $\Delta\eta$.

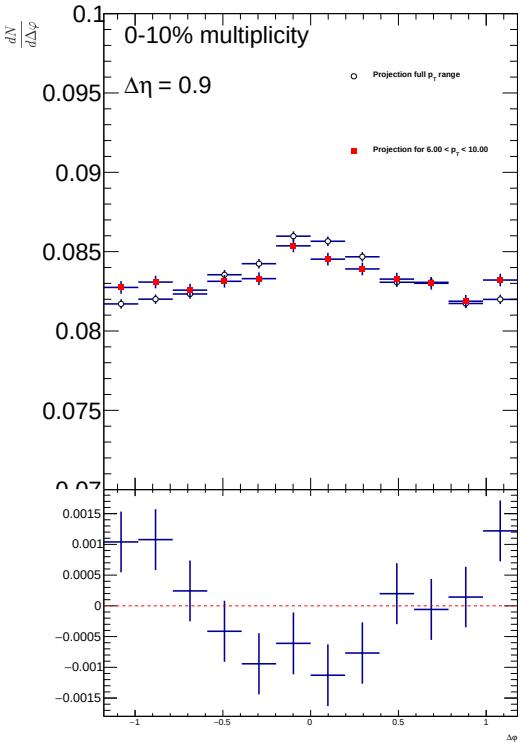


**(a)** The bump around $\varphi = 0$ is clearly visible for $\Delta\eta = 0.9$

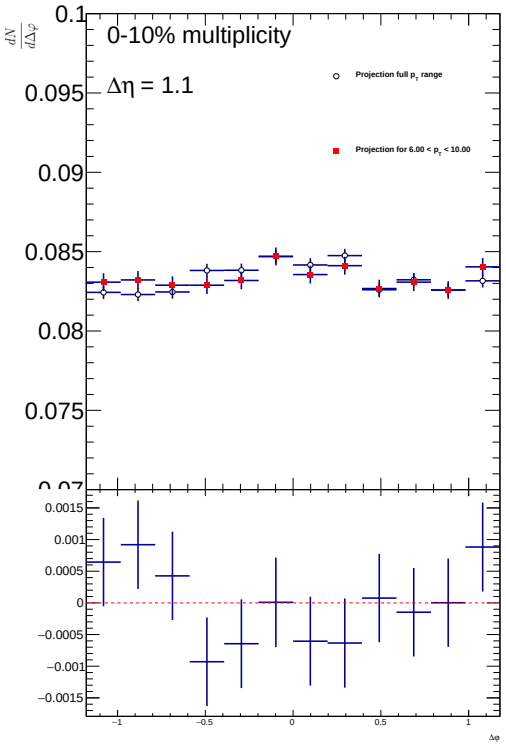


**(b)** The bump around $\varphi = 0$ diminished for $\Delta\eta = 1.1$

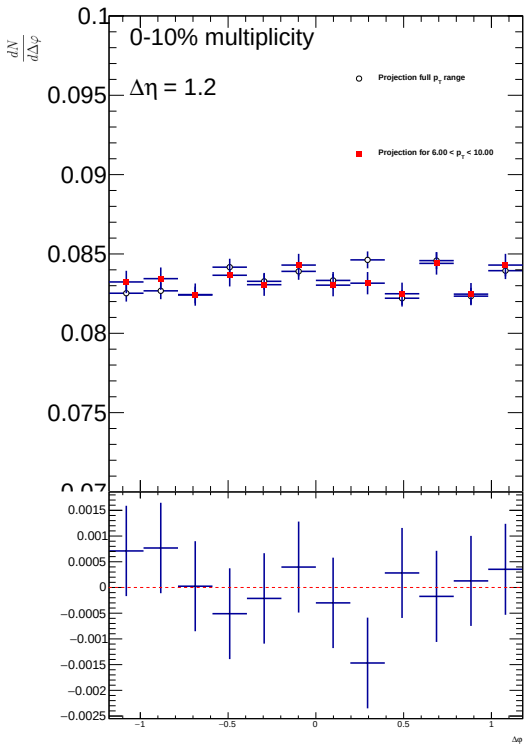


**(c)** The bump around $\varphi = 0$ disappears for $\Delta\eta = 1.2$

**Figure B.3:** Projected distribution of $\Delta\varphi$ across the entire $p_{\mathrm{T}}$ range, focusing on the 0-10% multiplicity range, with variations on $\Delta\eta$.

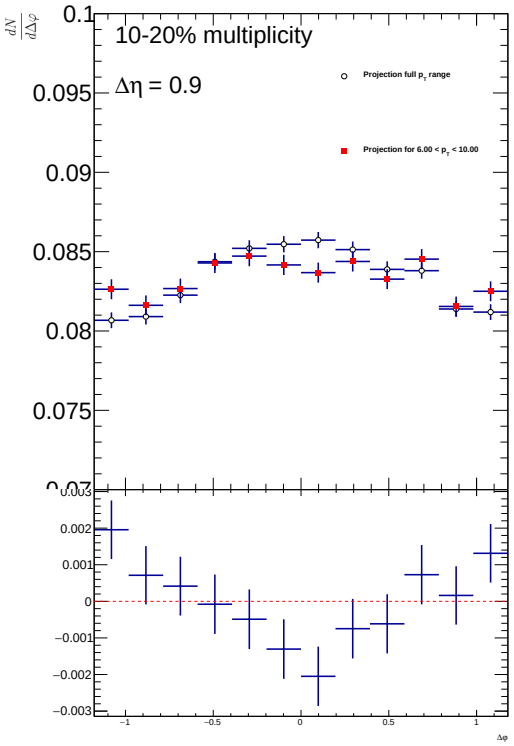


**(a)** The bump around $\varphi = 0$ is clearly visible for $\Delta\eta = 0.9$

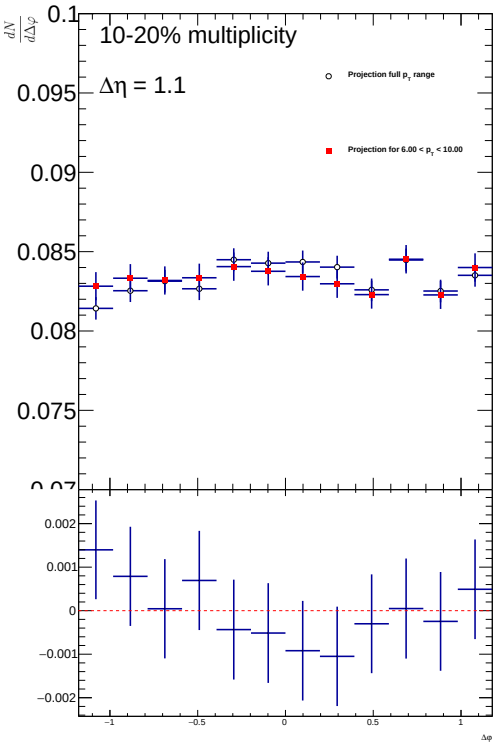


**(b)** The bump around $\varphi = 0$ diminished for $\Delta\eta = 1.1$

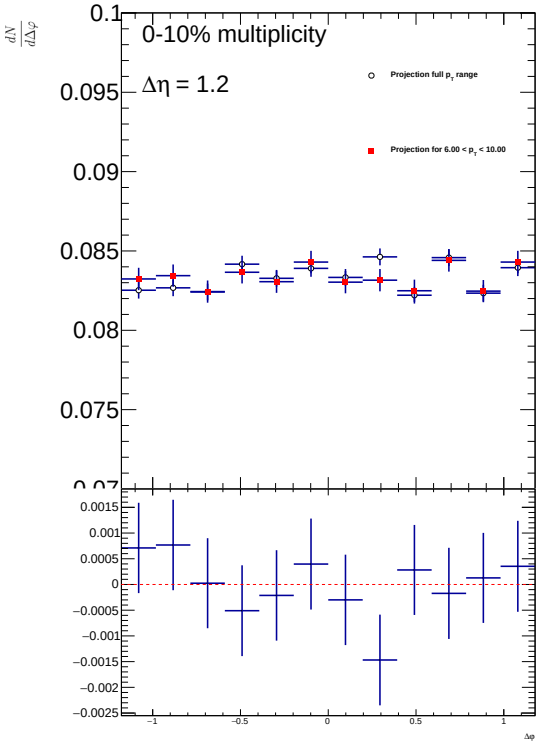


**(c)** The bump around $\varphi = 0$ disappears for $\Delta\eta = 1.2$

**Figure B.4:** Projected distribution of $\Delta\varphi$ across the entire $p_{\mathrm{T}}$ range, focusing on the 10-20% multiplicity range, with variations on $\Delta\eta$.

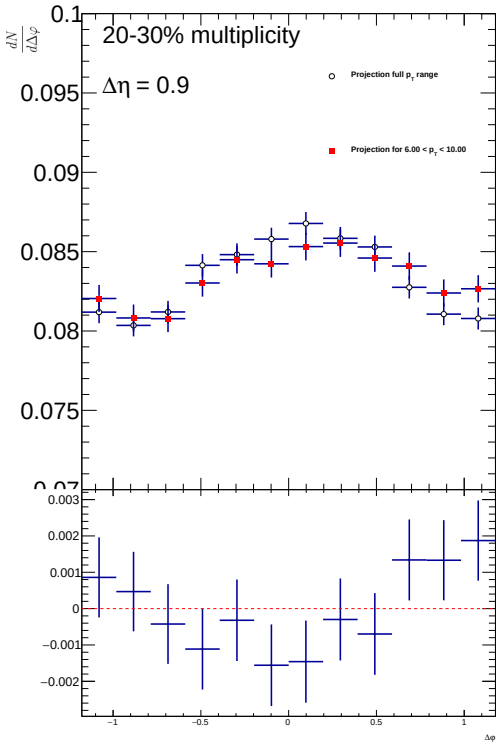


**(a)** The bump around $\varphi = 0$ is clearly visible for $\Delta\eta = 0.9$

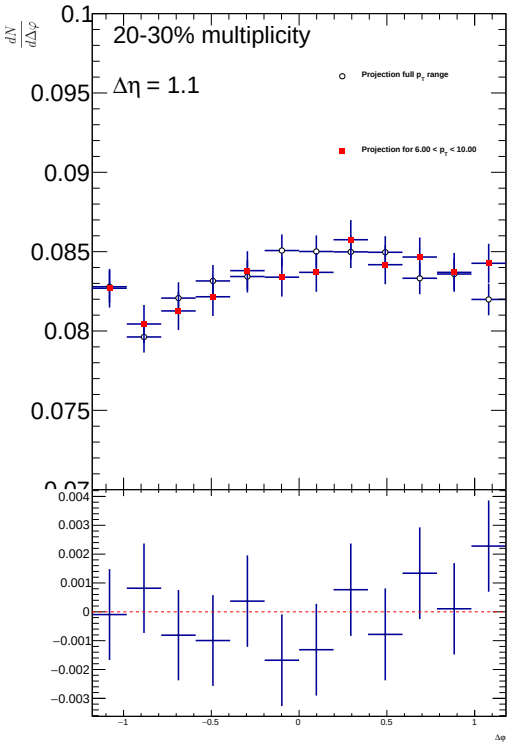


**(b)** The bump around $\varphi = 0$ diminished for $\Delta\eta = 1.1$

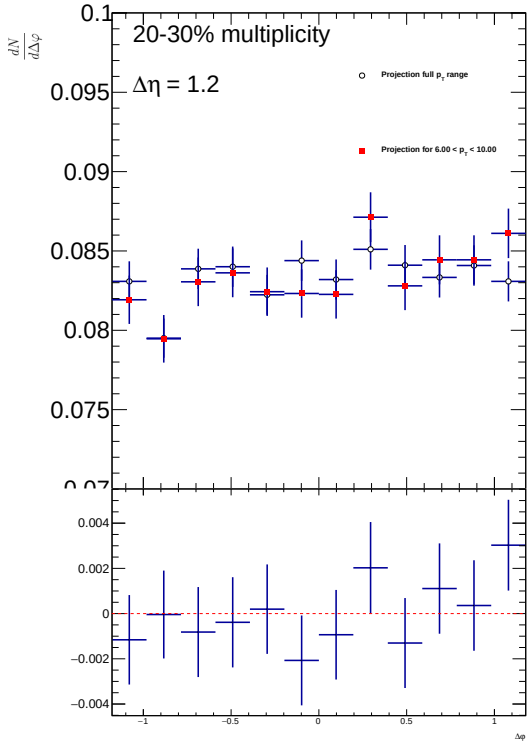


**(c)** The bump around $\varphi = 0$ disappears for $\Delta\eta = 1.2$

**Figure B.5:** Projected distribution of $\Delta\varphi$ across the entire $p_{\mathrm{T}}$ range, focusing on the 20-30% multiplicity range, with variations on $\Delta\eta$.

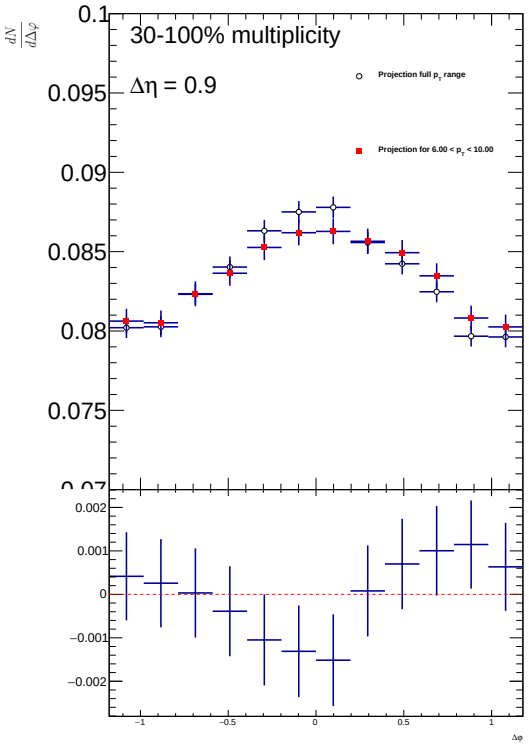


**(a)** The bump around $\varphi = 0$ is clearly visible for $\Delta\eta = 0.9$

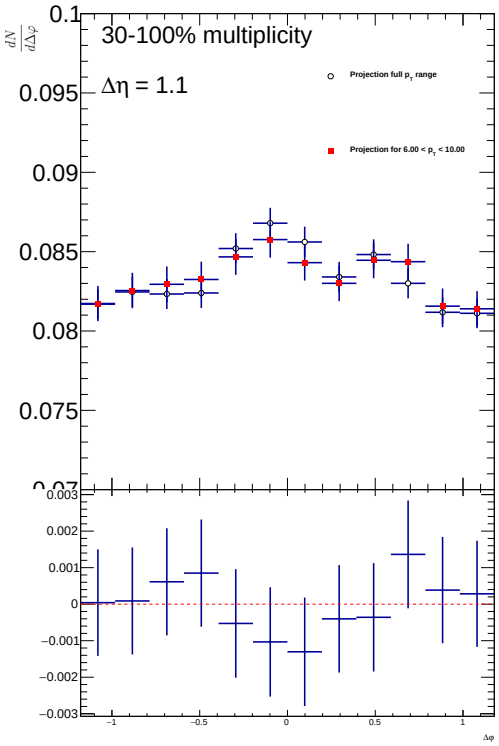


**(b)** The bump around $\varphi = 0$ diminished for $\Delta\eta = 1.1$

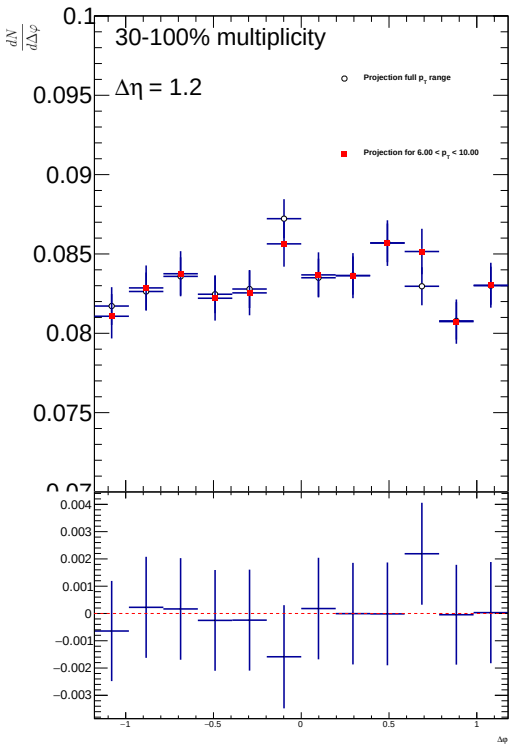


**(c)** The bump around $\varphi = 0$ disappears for $\Delta\eta = 1.2$

**Figure B.6:** Projected distribution of $\Delta\varphi$ across the entire $p_{\mathrm{T}}$ range, focusing on the 30-100% multiplicity range, with variations on $\Delta\eta$.